

FINAL REPORT

Project Title: BWR Assembly Optimization for Minor Actinide Recycling

Covering Period: October 1, 2005 – June 30, 2009

Date of Report: 22 March 2010

Recipient: University of Cincinnati
PO Box 210225
Cincinnati, OH 45221-0627

Award Number: DE-FC07-05ID14653

Subcontractor: G. Ivan Maldonado, 865-974-7562, Ivan.Maldonado@utk.edu

Other Partners: ORNL, LANL, Westinghouse Electric Co.

Contact(s): PI: John M. Christenson, 513-556-2002, John.Christenson@uc.edu

Project Team: J.P. Renier (ORNL), T.F. Marcille (LANL), J. Casal (Westinghouse)
Admin/Officers: Ron Fellows and Kenny Osborne (DOE), Sue Cutter (UC)

Project Objective:

The primary objective of the proposed project is to apply and extend the latest advancements in LWR fuel management optimization to the design of advanced boiling water reactor (BWR) fuel assemblies specifically for the recycling of minor actinides (MAs).

Background:

A top-level objective of the Advanced Fuel Cycle Systems Analysis program element of the DOE NERI program is to investigate spent fuel treatment and recycling options for current light water reactors (LWRs). Accordingly, this project targets to expand the traditional scope of nuclear fuel management optimization into the following two complementary specific objectives: (1) To develop a direct coupling between the pin-by-pin within-bundle loading control variables and core-wide (bundle-by-bundle) optimization objectives, (2) to extend the methodology developed to explicitly encompass control variables, objectives, and constraints designed to maximize minor actinide incineration in BWR bundles and cycles.

The first specific objective is projected to “uncover” dormant thermal margin made available by employing additional degrees of freedom within the optimization process, while the addition of minor actinides is expected to “consume” some of the uncovered thermal margin. Therefore, a key underlying goal of this project is to effectively invest some of the uncovered thermal margin into achieving the primary objective.

Background on Project Administration:

Due to a programmatic phase-out of the nuclear and radiological engineering program at the University of Cincinnati, the sole principal investigator (PI) and the two Ph.D. students specifically involved in this project moved from the University of Cincinnati to the University of Tennessee (UT) in the fall of 2007. Subsequently, to facilitate this project to continue, a research subcontract was extended by the University of Cincinnati to the University of Tennessee. The sub-agreement between the two universities involved was completed during the first quarter of 2008 and became effective in early 2008. The change of venue for the key participants and contractual logistics caused a few delays, however, the work on this project has continued. More recently, the parent project (and subcontract) was provided a no cost extension through June, 30, 2009.

In addition to the participants in this project, the computer equipment (22-Node Beowulf Cluster) and associated software license agreements with the Westinghouse Electric Co. (PHOENIX/POLCA/CM2 BWR codes) and NC State University (FORMOSA-L) have been transferred to UT and re-executed, respectively. Also, the primary collaborators at Oak Ridge National Laboratory are now physically more conveniently located relative to the research team. Therefore, multiple key steps have been taken and were implemented to seamlessly continue this research project from the University of Tennessee.

The report herein provided summarizes the results achieved through June 2009, particularly those results and advancements reported by the primary Ph.D. students supported by this grant, namely, Mr. Jack Galloway and Mr. Hermilo Hernandez. However, it should be noted that the development of a comprehensive actinide tracking capability for LWRs will continue ahead.

1. Introduction

Background

While nuclear energy continues to prove to be a major player as an electricity source in the world and here in the United States, one of the main outstanding controversies in public perception continues to be the treatment of spent nuclear fuel, often referred to as nuclear *waste* despite the fact it is by and large an untapped and valuable resource. Accordingly, several options to deal with spent nuclear fuel have been proposed; ranging from full recycling, to separations and recycling of certain components, to long-term storage of all constituents. Most recently, however, multi-billion dollar efforts originally directed toward the long-term storage of US nuclear waste in facilities such as Yucca Mountain have apparently dwindled to a halt while the current administration and the US Department of Energy devise a new strategy toward nuclear waste disposal. In principle, this change in direction promotes a more careful evaluation of recycling options.

When discussing potential recycling scenarios, much effort has been put forth recently into recycling in fast reactors; while there has been a less concerted effort invested into the potential of using the existing fleet of light water reactors (LWRs) as drivers for recycling of spent fuel waste components. The main underlying assumption is that higher energy (fast) neutrons are more efficient at transmuting a larger variety of transuranic isotopes. However, in practice, operating fast reactors do not exist in the US and the likelihood of such facilities being built is quite low and surrounded by large uncertainties. Meanwhile, our country successfully operates 104 LWRs that could realistically be employed to help mitigate some of the problems associated with nuclear waste.

As seen in Figure 1.1, in the 1 to 100 year time frame after the discharge of spent fuel, fission product activity is the dominating contributor to heat generation and radiotoxicity from spent fuel; while the contribution due to actinide decay becomes the dominating contributor during the

100 to 1000 year period and beyond. The greatest contributor to actinide activity during the 100 to 1000 year time frame is americium-241 (^{241}Am).

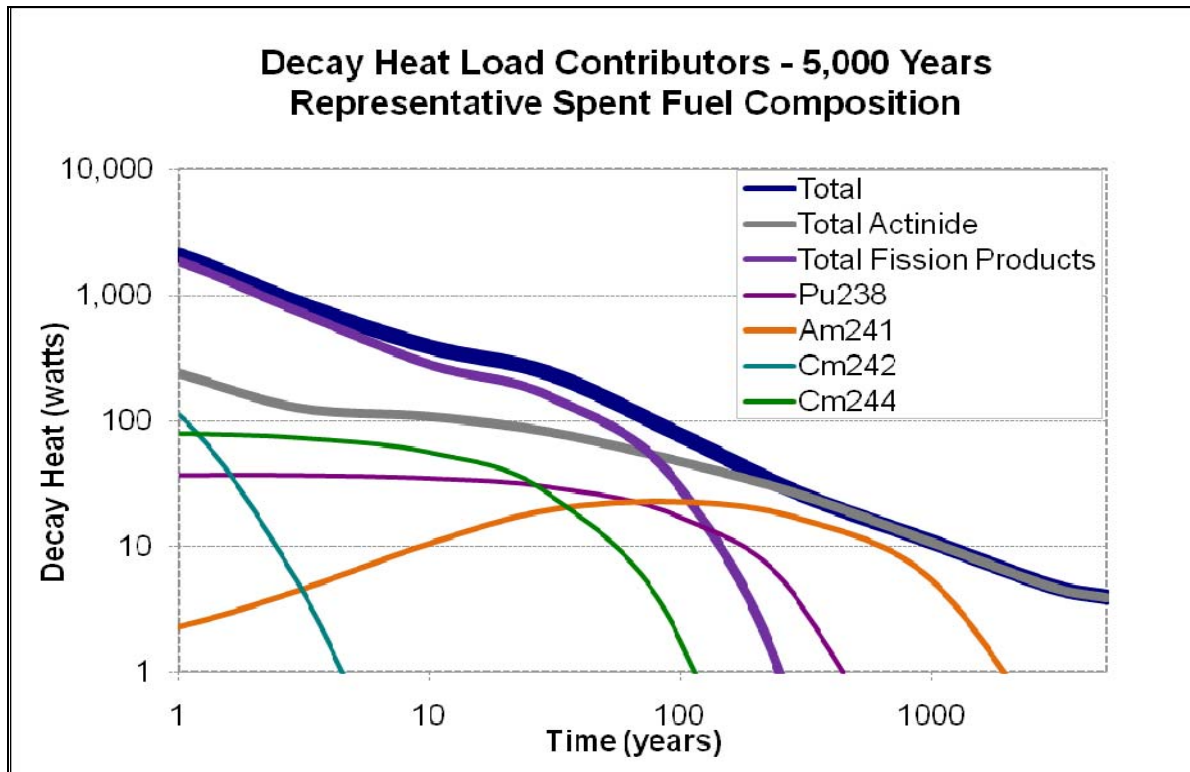


Figure 1.1 Contribution to Heat Load in Spent Nuclear Fuel

Several options exist for managing fission products; given their relatively short half-lives in comparison to those of the actinides, separation and storage can be an adequate path. Alternatively, transmutation in fast reactors has also been proposed. Likewise, dealing with plutonium isotopes via recycling in thermal or fast reactors or as mixed oxide (MOX) fuel are technically mature areas in which much research has been invested over the years.

Among several objectives, this project proposes incineration of the most active and long-lived minor actinides, americium-241, by employing the existing fleet of operating boiling water reactors (BWRs). One of the underlying hypotheses is to try to exploit the significant boiling in the upper region of a BWR core. Although a BWR exhibits a standard thermal neutron spectrum in the lower portion of the core, it promotes a harder neutron spectrum in the upper region of the

core. This spectral shift could be utilized to preferentially load americium or other actinides at the appropriate axial levels for optimum spectral utilization for incineration.

Accordingly, via collaboration with the Westinghouse Electric Co., this research project provides substantial proof-of-principle of the ability to efficiently incinerate recycled minor actinides such as americium-241 (as heterogeneous targets) in a BWR by employing commercial-grade three-dimensional core design simulation tools for the analysis. This first-of-its-kind study is described in detail in Chapter 2.

Next, while in the process of assessing available tools and their various constraints, this project also addresses a major hurdle encountered while evaluating the viability of recycling scenarios in a BWR, which is the lack of available three-dimensional BWR core simulation codes with the capability to provide detailed isotopic information for a wide variety of isotopes, including the full suite of transuranics; neptunium, plutonium, americium, and curium. In fact, the typical core simulators available for performing such a study tend to contain a very limited output of isotopic information only reporting a select number of plutonium, neptunium and americium isotopes (with no curium isotopes generally available or tracked). As a result, the development of a tool capable of modeling a BWR while also tracking a complete description of node-by-node isotopics became an additional though major focus of this project.

Through collaboration with NC State University and under sponsorship by Oak Ridge National Laboratory this project also became linked to the integration of the NESTLE 3D PWR core simulation software [27] to the SCALE/TRITON lattice physics and core depletion sequences [16]. In fact, this collaboration provided a perfect platform and launching pad to pursue the development of a BWR simulator, and to ultimately seek its integration to the world-renowned ORIGEN depletion capabilities on a node-by-node basis. This work requires two major components. First, the development of a thermal-hydraulic module capable of capturing sub-cooled void fraction, as well as accurately modeling the void fraction in the bulk boiling phase. Secondly, the implementation of a scheme for tracking a wide number of isotopes on a nodal basis, within the scope of a “traditional” three-dimensional core simulator.

The thermal hydraulic developments to upgrade the NESTLE code from a reliable PWR simulator to a BWR simulator are discussed in Chapters 3, while the validation of the BWR simulator is presented in Chapter 4. Finally, the work related to the integration of NESTLE to ORIGEN is discussed in Chapter 5.

Literature Review

Transmutation

For several decades the nuclear industry in the United States has marched forward with the expectation that the spent nuclear fuel, which is currently stored on-site at power plant locations, would end up permanently stored in the Yucca Mountain site currently under construction. Due to a combination of political struggles, environmental concerns, and the potential for recovering energy from the spent nuclear fuel, this expectation has been waning somewhat. Due to this, the investigations of alternate routes for handling spent nuclear fuel have begun. Transmutation in reactor environments have started to be investigated, including fast reactors, thermal reactors and sub-critical accelerator driven transmutation.

In researching the literature surrounding actinide transmutation, several studies were found assessing the viability of actinide transmutation using both light water reactors (LWRs) and fast reactors. The majority of the studies focused on two-dimensional simulations performed with two dimensional codes akin to lattice-physics codes, or using MCNP based simulations. These studies have been beneficial for determining which isotopes are well suited to incineration in a fast spectrum and which are well suited to incineration in a thermal spectrum, but leave significant uncertainties surrounding the viability of in-core and multi-cycle fuel management and the practical implementation within modern day LWRs. Not surprisingly, for a number of valid reasons, it was also observed that there is a strong research base in this area from outside the United States, although several excellent resources were found originating in the U.S.

According to Varaine and Zaetta [28] recycling in LWRs is a possibility for a limited number isotopes, due to the thermal cross-sections of various actinides; where the study was confined to

study PWR transmutation models, where the spectral shift characteristic of a BWR was not investigated. Promising results were obtained and this feasibility study for actinide transmutation was based in France, where the PWR is the nuclear reactor of choice, and where France has been a leader in separations and transmutation of mixed-oxide (MOX) fuels for decades. Irrelevant of the background, that research illustrated that thermal reactor transmutation is technically feasible in PWRs, while the effects in BWRs and via three-dimensional nuclear fuel management evaluations were not part of that study.

Considerable experience exists in the recycle of plutonium in LWRs, primarily in Europe and Japan. In the United States, the recycle of weapons-grade material into LWRs in the form of MOX fuel is planned and lead-test assemblies with MOX fuel have been loaded in the Duke Power Catawba nuclear reactor. Thus, the use of MOX fuel for burning plutonium has been demonstrated. The introduction of other actinides such as Np, Am, and Cm, into LWR fuel, however, has not yet been established and presents several challenges in manufacturing, handling, and transportation aspects, in addition to impacts upon reactor performance.

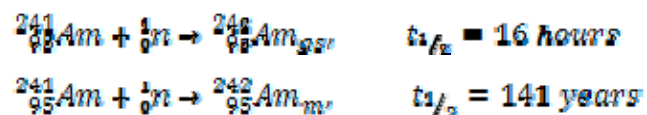
Several studies have been performed to evaluate homogeneous and heterogeneous recycling options. Much of that work is well summarized in a compendium report by Taiwo and Hill [26] which provides additional references to a number of detailed reports on the CORAIL, CONFU, Inert-Matrix, and various other heterogeneous and homogenous recycling strategies. The research performed so far provides an excellent overview of the potential of LWR recycling strategies. Most of the prior research, however, does not typically include full-core analyses and does not focus upon BWRs, which are key emphases of the research herein reported in what pertains to americium-spiked lattices and bundles.

With regard to the potential for using BWRs in this capacity, as it was earlier shown by Erighin and Maldonado [5] with the MCNP and MONTEBURNS codes, similarly; François and Guzman [7] have shown some promising studies at the lattice level, using the lattice physics code HELIOS with the intention of developing a fuel design intended to use minor actinide loading to supplant traditional burnable absorbers. Clearly observed in these research studies is that the behavior of k_{∞} as a function of burnup is dramatically different relative to the typical behavior

seen in a lattice loaded with gadolinium as the burnable absorber, the hot excess reactivity hold down is much lower due to the significant differences in thermal absorption cross-sections. Despite these differences, the potential to incinerate long-lived actinides was illustrated. However, the next step of accommodating actinide loaded bundles into core loading patterns and the impact on core behavior needs to be understood. Likewise, it is important to note that while these prior studies showed promise at the lattice level, a lack of a comprehensive tool and study of the impact upon core-wide thermal and reactivity limits as well as the corresponding three-dimensional transmutation needs to be investigated.

Similarly, Hernandez and Maldonado [10] [11] have demonstrated success in designing BWR lattices and tools for optimizing actinide transmutation. However, the process of optimizing fuel bundles and core reload designs for actinide transmutation, while satisfying operational constraints is still a non-existent capability. Additionally, Raites, et al. [20] have also performed studies pertaining to the feasibility of using BWRs as transmutation drivers, among other things; investigating the effect that void fraction has on the transmutation effect. While this study did not focus particularly on Americium-241, the dominant contributor to the heat load from 100-1000 years, it again buffers the feasibility of using BWR cores for such transmutation. As seen throughout these studies, the lack of a robust and available tool to perform three-dimensional in-core and multi-cycle fuel analysis, as well as a generalized isotopic tracking is evident. While many studies are performed at the lattice level, or using an extension of lattice results to potential core-wide results, the lack of a tool capable of simulating in-core fuel behavior as well as isotopic changes is clear.

While discussing a thermal neutron spectrum as an avenue for the transmutation of americium 241, it is helpful to point out how this occurs. Americium 241 is transmuted via capture through one of the two following reactions:



Fortunately, the fission cross-section for both states of Am-242 is favorable for incineration. At 0.0253 eV the total fission cross-section for the ground state is ~2100 barns, whereas at the same conditions, the total fission-cross section for the meta stable state is ~6700 barns [12] . Given these high values of the thermal fission cross-section, relative to that of U-235 at 582 b, the ability to incinerate this high heat-load component of spent fuel in a thermal spectrum appears quite viable. While in the past there was varying nuclear data surrounding the ground state fission cross-section, due to its short half-life, the various nuclear data files have come into close agreement regarding the cross-section of Am-242 ground state, which is of fundamental importance for any nuclear computer simulation. Fioni, et al. [6] have demonstrated the ability to incinerate Am-241 with thermal neutrons, with success, leading them to the conclusion “the Am-242gs capture cross section keeps the option to transmute Am-241 together with the minor actinides issued from multi-recycling of a MOX fuel by an intense flux of moderated neutrons”. This provides the key requirement for transmutation, as there are numerous reactors worldwide capable of providing an intense flux of moderated neutrons, and since Am-242gs readily fissions in this environment the potential is evident.

With respect to transmutation of various isotopes in a thermal environment, one major factor is the inventory of the highly transmutable isotopes. For instance, Americium-241 is advantageous for transmutation in a thermal environment through the capture reaction, followed by the fission of Am-242. Other isotopes are not nearly as favorable, such as Pu-241. When placed in a thermal environment, Pu-241 will capture a neutron, becoming Pu-242 which does not have an advantageous path towards incineration or transmutation, but rather tends to lead to higher and heavier actinides, which are unfavorable. One way to treat this is to leave spent nuclear fuel (SNF) to “cool” for 30 years or more after being used in-core. In this way, given the 14 year half life of Pu-241 which beta decays to Am-241, approximately 75% of the original inventory of Pu-241 has converted to the transmutable Am-241, while the initial inventory of Am-241 is relatively unchanged given its long half-life on the order of 430 years. Collins, Renier, DelCul and Spencer [3] have performed calculations detailing and investigating the effect of this cooling time, using two simulations; one simulation performed with a 30 year cooling time, and another

simulation with a 5 year cooling time. In addition, a comparison of the production and destruction rates of several of the key transuranics was performed when using an ABR (advanced burner reactor) versus a light water reactor. The results of this study again showed promising results for the potential incineration of various minor actinides, in particular Americium 241, in a thermal flux environment. Studies, such as the aforementioned study, as well as the work done by Collins and Renier [4] Zaetta [30] as well as numerous other sources have discussed the potential need for a two-fold transmutation system, comprised of recycling in both fast reactor and thermal reactor environments. As mentioned before, this appears to be a potentially advantageous scenario as it takes advantage of, at least in part, the infrastructure already in place as well as allows for the recovery of much of the unused energy still present in spent nuclear fuel. The lack of a capability for simulating actinide loaded bundles burned in BWR core loading patterns that satisfy thermal limits (shut down margin for instance) and represent appropriate conditions for several cycles as well as accurately evaluating the transmutation of actinides is again encountered.

Of particular interest, and observed in the literature, are the conflicting approaches regarding the most effective reactor type for the incineration of various plutonium isotopes. Historically, the practice of loading MOX bundles in LWR cores has been carried out, thus many reports point to recycling plutonium in the light water reactor while recommending the other actinides be transmuted in a fast reactor. That said, however, several other reports comment that the most efficient process may be a partial inversion of this, whereby plutonium isotopes end up in a fast reactor while some of the higher actinides (such as Am-241) are best transmuted in a thermal reactor. This indicates that more detailed evaluation tools are needed to study the inherent changes due to loading new materials in nuclear fuel, the different in-core behavior, and the practical limitations on the volume of new materials that can be safely loaded in a core while satisfying operational limits. Thus, an available, efficient, and accurate tool for analyzing BWR core behavior with a generalized tracking of isotopic inventories provides a new and significant contribution to the newly emerging field of LWR recycling and actinide management.

Thermal-Hydraulics

In order to develop a code capable of solving representative steady state BWR operating conditions, one major component is a robust steady state two-phase flow solution scheme. Several options exist for solving two-phase flow conditions. RELAP5-3D [22] uses a model described as follows:

“The RELAP5-3D hydrodynamic model is a transient, two-fluid model for flow of a two-phase vapor/gas-liquid mixture that can contain noncondensable components in the vapor/gas phase and/or a soluble component in the liquid phase. A one-dimensional as well as a multi-dimensional hydrodynamic model is included in the code.”

While the RELAP5-3D approach is certainly among the state of the art in two-phase flow analysis, the desired thermal-hydraulic solution for this BWR core design applications needs not be a robust solver applicable to transient conditions, but rather one that handles stead-state flow characteristics accurately and quickly. Another influencing factor was the lack of need for a multi-dimensional solution. Given the boxed (fuel channel) design in BWR bundles, the flow is essentially a vertical flow, thus a one-dimensional capability is sufficient. Finally, the time requirements for achieving convergence in such a solution scheme can be high, and since each channel was going to be modeled independently leading to upwards of 800 channel solutions, an alternate solution algorithm was pursued in contrast to the current wave of coupled neutronic and thermal hydraulic efforts [29] .

Numerous and modern industrial BWR simulation codes utilize the drift-flux model as their approach to two-phase flow computation within their core simulators. The accuracy of steady-state solutions has been well documented, as well as the speed of convergence when compared to distinct two-fluid models. In addition, in the development of the BWR analysis and optimization tool FORMOSA-B, Moore [17] utilized the drift-flux solution scheme as the thermal-hydraulic solution algorithm of choice, yielding good results in relatively short amounts of computational time. While no doubt a valuable tool for BWR analysis, FORMOSA-B is neither publicly available, nor capable of tracking the necessary number of isotopes needed for transmutation analyses, as well as tracking the inventories of other isotopes that build-up during reactor

operation. In addition to FORMOSA-B, many other private companies utilize the drift-flux method as their solution algorithm of choice for steady state conditions; such as GE's PANACEA code, Studsvik's SIMULATE code [25] , and Westinghouse's POLCA code, as a few examples. However, all of these methodologies are company proprietary and unavailable to the public. In essence, if one wants to have a two-phase flow drift-flux model embedded into a core simulator, one has to develop it, implement it, and validate it.

Isotopics

In searching for simulation tools to use for analysis, no viable and available three-dimensional core simulators were found that could both accurately model a BWR, as well as give the necessary isotopic inventories for the actinides of interest. While codes such as MONTEBURNS [19] added the capability of ORIGEN-caliber isotopic tracking to the MCNP code; attempting to analyze a large BWR core (700-800 bundles) with these tools is computationally daunting, not to mention that they don't have the capability of modeling thermal hydraulic feedbacks. While Monteburns may not be the computational tool to use for developing and analyzing BWR core loading patterns the employment of ORIGEN as the computational tool for isotopic evaluations is an insightful and helpful approach. Thus, applying a similar approach to call the latest available version of ORIGEN [8] on a nodal basis within the paradigm of a traditional BWR core simulator is herein pursued as a unique objective, as in fact, no such capability exists within modern 3D LWR simulators.

2. Proof of Principle Studies

Initial studies on the feasibility of the transmutation of Americium 241 the thermal spectrum of a BWR yielded positive results. The first step of a proof of principle study incorporated using the three-dimensional core simulator Polca, a product of Westinghouse Electric Co. Using an initial core loading pattern provided with the code as a starting point, four bundles spiked with Americium 241 were loaded into a central location of the core. The four bundles loaded in the core were generated via the lattice physics optimization code FORMOSA-L, which had been adapted to include an optimization option for americium transmutation [10] [11] An overview of this process, including core loading is shown in the following Figure 2.1.

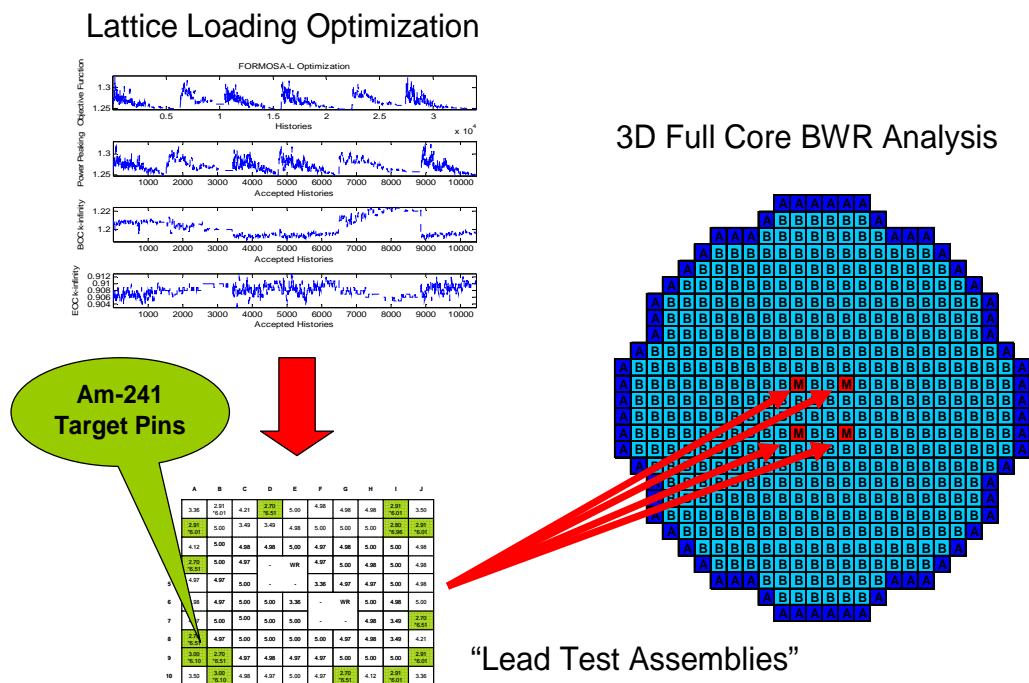
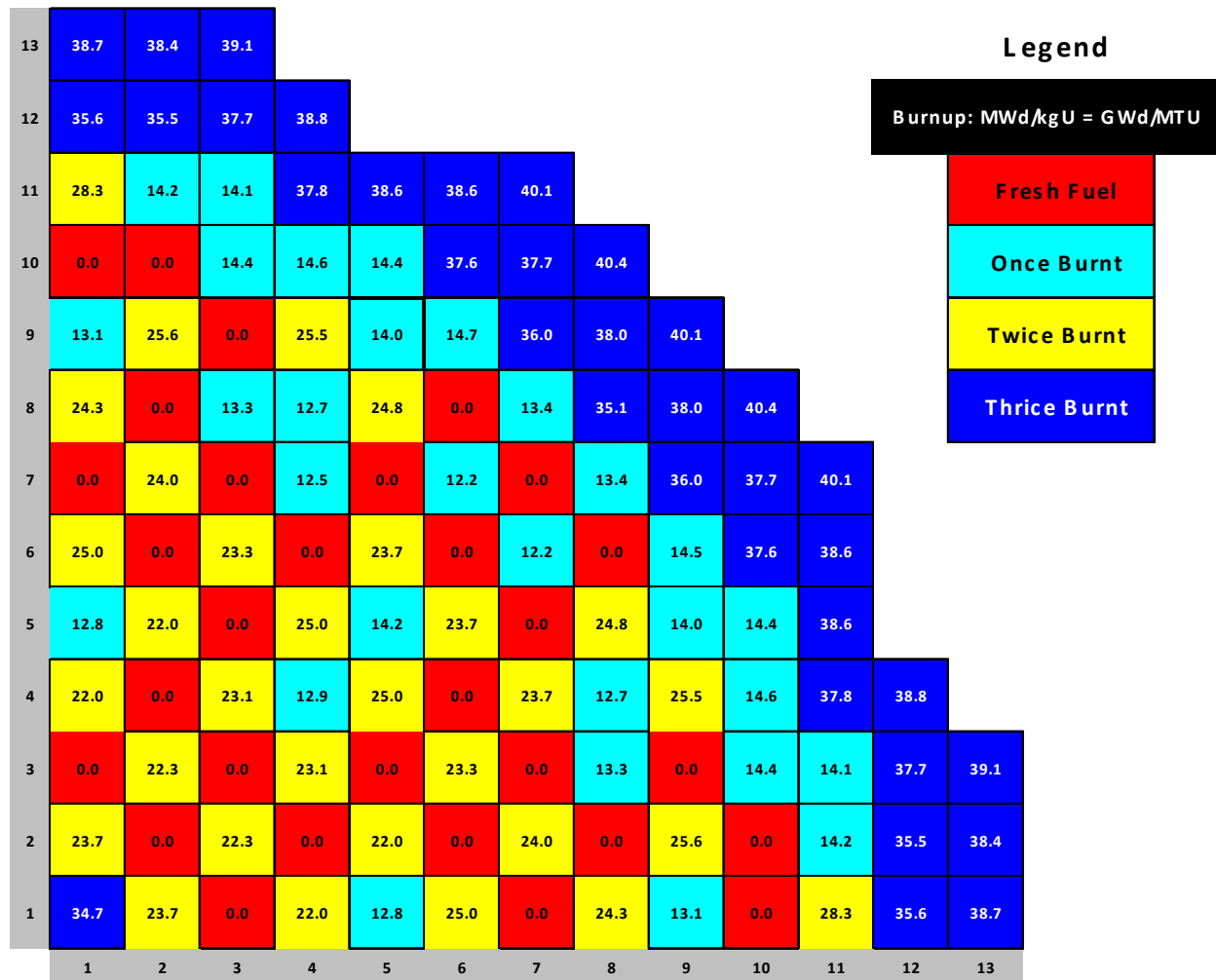


Figure 2.1 Lattice to Core Process

In order to simulate pseudo-equilibrium conditions; three cycles were simulated whereby the entire core of non-spiked bundles was removed and reloaded, while the 4 spiked bundles remained in their noted positions. Simulations with burnups higher than 30 GWD/MTU showed promising results with respect to americium transmutation.

During the simulations using the initial core loading pattern given and inserting spiked bundles several unfavorable thermal margin results were observed, primarily in the neighborhood of the 4 spiked bundles, where severe power peaking was observed. In practice, this was the result of loading much higher enriched bundles (>4% enriched) in central locations in a core where every other bundle was enriched to 1.94% (characteristic of an initial core). Thus, it was determined that a more representative core loading pattern was needed to more accurately assess the level of transmutation that could be achieved in a modern BWR core, as well as to model a more realistic impact upon reactivity margins.

No publicly available core loading strategies were found that suited the purpose, as these are generally tightly controlled and proprietary to vendors and utilities, therefore, we developed a realistic core loading pattern that could be led to an equilibrium state. The fuel bundle used was created in-house, which compared very favorably against an industry standard bundle used as a benchmark. The following Figure 2.2 shows a quarter core slice of the loading pattern and the burnup values of the bundles in-core.



The bundle used for this simulation was comprised of four major zones. The bottom axial zone containing natural uranium, followed by a dominant zone featuring gadolinium loaded pins for reactivity suppression, followed by a vanishing zone where part-length rods end, finally a natural uranium top, also with vanished rods; shown below in figure Figure 2.3.

Upper Blanket with vanishing zone (6.9")

0.71	0.71	0.71	0.71	0.71	0.71	0.71	0.71	0.71	0.71
0.71	VAN	0.71	VAN	0.71	VAN	0.71	VAN	0.71	0.71
0.71	0.71	0.71	0.71	0.71	0.71	0.71	0.71	0.71	0.71
0.71	VAN	0.71	0.71	0.71	H2O	H2O	0.71	VAN	0.71
0.71	0.71	0.71	0.71	VAN	H2O	H2O	0.71	0.71	0.71
0.71	0.71	0.71	H2O	H2O	VAN	0.71	0.71	0.71	0.71
0.71	VAN	0.71	H2O	H2O	0.71	0.71	0.71	VAN	0.71
0.71	0.71	0.71	0.71	0.71	0.71	0.71	0.71	0.71	0.71
0.71	VAN	0.71	VAN	0.71	0.71	VAN	0.71	VAN	0.71
0.71	0.71	0.71	0.71	0.71	0.71	0.71	0.71	0.71	0.71

Upper Blanket

Upper Vanishing Zone (42")

2.00	2.80	3.60	4.40	4.40	4.40	3.95	3.60	2.80	2.00
2.80	VAN	3.95	VAN	3.95	3.95	VAN	3.95	VAN	2.80
3.60	3.95	4.40/5.00	3.95	4.40/5.00	4.90	4.40	4.40/4.00	3.95	3.95
4.40	VAN	3.95	4.40/2.00	4.90	H2O	H2O	4.40	VAN	4.40
4.40	3.95	4.40/5.00	4.90	VAN	H2O	H2O	4.40/5.00	4.40	4.40
4.40	3.95	4.90	H2O	H2O	VAN	4.40	4.40	4.40/4.00	4.40
3.95	VAN	4.40	H2O	H2O	4.40	4.40	4.40/4.00	VAN	4.40
3.60	3.95	4.40/4.00	4.40	4.40/5.00	4.40	4.40/4.00	4.40	3.95/4.00	3.95
2.80	VAN	3.95	VAN	4.40	4.40/4.00	VAN	3.95/4.00	VAN	3.60
2.00	2.80	3.95	4.40	4.40	4.40	4.40	3.95	3.60	2.00

Vanishing Zone

Lower Dominant Zone (90")

2.00	2.80	3.60	4.40	4.40	4.40	3.95	3.60	2.80	2.00
2.80	4.40	3.95	4.90	3.95	3.95	4.90	3.95	4.40	2.80
3.60	3.95	4.40/5.00	3.95	4.40/5.00	4.90	4.40	4.40/4.00	3.95	3.95
4.40	4.90	3.95	4.40/2.00	4.90	H2O	H2O	4.40	4.90	4.40
4.40	3.95	4.40/5.00	4.90	4.40	H2O	H2O	4.40/5.00	4.40	4.40
4.40	3.95	4.90	H2O	H2O	4.40	4.40	4.40	4.40/4.00	4.40
3.95	4.90	4.40	H2O	H2O	4.40	4.40	4.40/4.00	4.90	4.40
3.60	3.95	4.40/4.00	4.40	4.40/5.00	4.40	4.40/4.00	4.40	3.95/4.00	3.95
2.80	4.40	3.95	4.90	4.40	4.40/4.00	4.90	3.95/4.00	4.40	3.60
2.00	2.80	3.95	4.40	4.40	4.40	4.40	3.95	3.60	2.00

Dominant Zone

Lower Blanket (6")

0.71	0.71	0.71	0.71	0.71	0.71	0.71	0.71	0.71	0.71
0.71	0.71	0.71	0.71	0.71	0.71	0.71	0.71	0.71	0.71
0.71	0.71	0.71	0.71	0.71	0.71	0.71	0.71	0.71	0.71
0.71	0.71	0.71	0.71	0.71	H2O	H2O	0.71	0.71	0.71
0.71	0.71	0.71	0.71	0.71	H2O	H2O	0.71	0.71	0.71
0.71	0.71	0.71	H2O	H2O	0.71	0.71	0.71	0.71	0.71
0.71	0.71	0.71	H2O	H2O	0.71	0.71	0.71	0.71	0.71
0.71	0.71	0.71	0.71	0.71	0.71	0.71	0.71	0.71	0.71
0.71	0.71	0.71	0.71	0.71	0.71	0.71	0.71	0.71	0.71
0.71	0.71	0.71	0.71	0.71	0.71	0.71	0.71	0.71	0.71

Lower Blanket

Figure 2.3 Equilibrium Core Bundle Design

Once loaded with fuel, the core was driven to an equilibrium state using a representative standard bundle, by performing 9 fuel burn and shuffle sequences. Once demonstrating equilibrium behavior, the spiked bundles were then loaded into 2 or 4 locations, referencing quarter core symmetry (thus 8 or 16 total bundles in-core). ²⁴¹Am transmutation was computed, as well as initial studies into possible effects on shutdown margin. For the first study using the equilibrium

core design, the spiked bundles were loaded into fresh fuel locations and then another equilibrium analysis was done, loading and shuffling for somewhere between 7-9 fuel burn and reshuffle sequences before equilibrium behavior was exhibited. The loading positions for the spiked bundles throughout the cycle are given below in Figure 2.4.

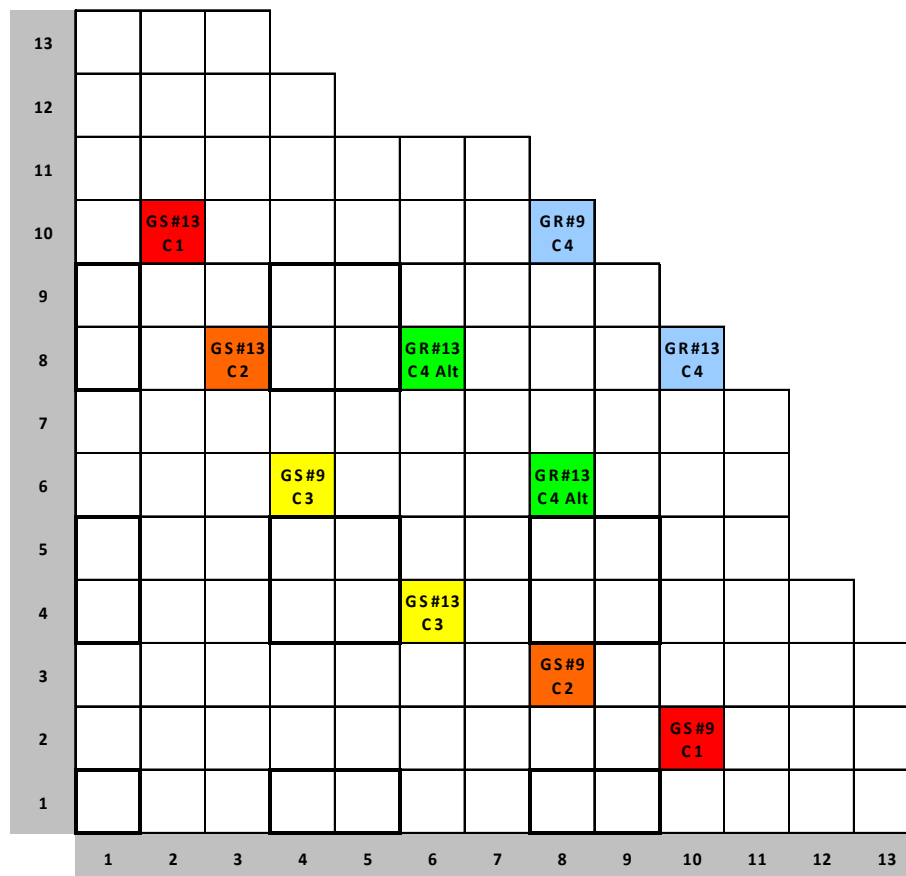


Figure 2.4 Spiked Bundle Locations

Two simulations were performed for cycle 4 of the spiked bundles, occupied by positions “C4” or “C4 Alt”. The difference here accounting for the difference between what industry would typically do with these high burnup bundles, as opposed to what would be best for transmutation. Utilities typically move the least reactive bundles to the core periphery, to maximize cycle length, hence where the “C4” bundles are placed. This would cause a limitation on the amount of Am-241 transmuted though, as the neutron flux is much lower on the periphery. As a

sensitivity study, these bundles were also placed in more central core locations to observe the difference in Am-241 transmutation as a result of bundle location at high burnup. Predictably the bundles in the “C4 Alt” positions encountered greater Am-241 transmutation. The difference was on the order of ~3-4% transmutation in the standard “C4” location as opposed to the “C4 Alt” position. The further discussion of where to put the bundles, and the economic penalty associated, would undoubtedly lie between the operating utility and those responsible for waste disposal.

Using the equilibrium analysis and core loading pattern described above, the total amount of Americium 241 destroyed throughout the cycle is shown below in Figure 2.5. Observe also that the expected amount of Americium 241 build up for a standard bundle is also included for reference.

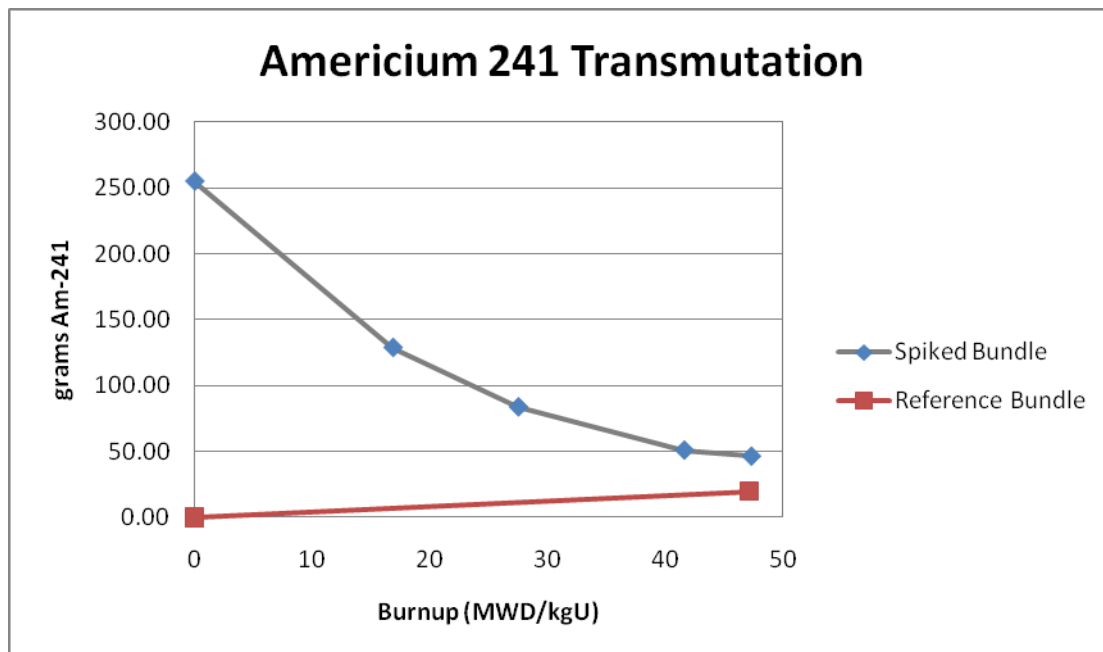


Figure 2.5 Spiked Bundle Americium 241 Transmutation

Observed is that a destruction of ~209g of Am-241 was destroyed in one spiked bundle when burned to ~50 MWD/kgU. Compare this to a standard accumulation of 20g of Am 241 due to production from U-238, and the percent of original Am-241 transmuted is ~91%. Thus, if two bundles were loaded in quarter core symmetry every reload and the batch size was ~1/3; for a

full core computation the transmutation that would be ~1700g of Am-241 destroyed every cycle, with a production of ~2500g. This results in a net production of 800g of Am-241 every cycle; however if 16 bundles were loaded every cycle (thus 4 bundles in quarter core symmetry), a total destruction of 3400g, thus a net destruction of 900g per cycle could be achieved.

One particular characteristic of the spiked bundles that deviates greatly from standard fuel designs is the lack of gadolinium as a reactivity control mechanism. In the design phase of the spiked bundles, it was decided upon to supplant the gadolinium loaded pins with the spiked pins. In order to achieve an end-of-life reactivity that is representative of current fuel designs it was necessary to have a higher U-235 enrichment than the gadolinium loaded counter-part. This is due to the U-235 burning out faster at beginning-of-life due to the absence of gadolinium, or any other reactivity suppression mechanism. As a result, the bundles end up being much hotter at beginning-of-life, which was a possible concern regarding shutdown margin for the cells in the neighborhood of the spiked bundle. A shutdown margin calculation was performed for the whole core, with the results given here in Figure 2.6.

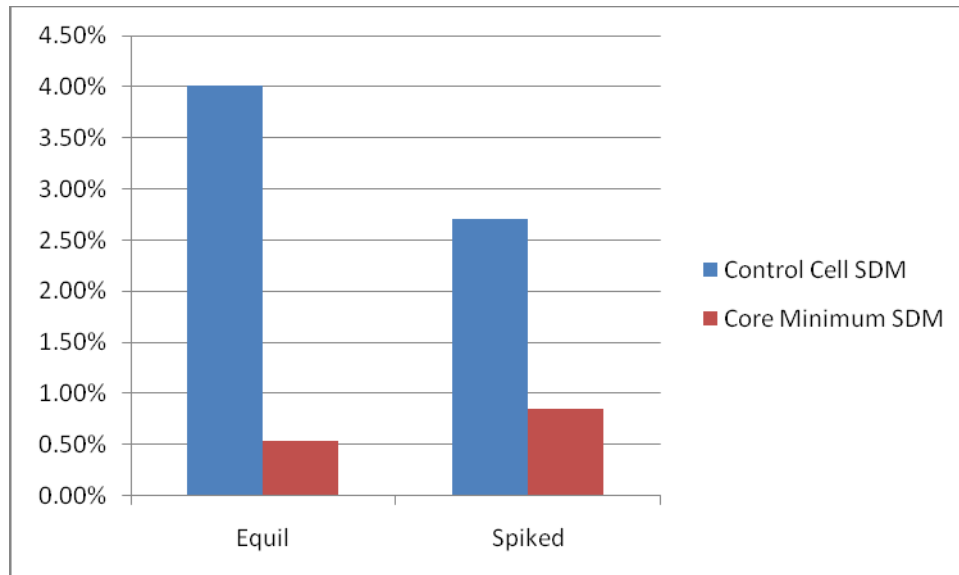


Figure 2.6 Equilibrium Core Shutdown Margin

While the limiting condition for shutdown margin actually increased (yielding more safety margin) for the whole core scenario, this is a large function of the loading pattern and control rod

pattern used and should not be seen as an inherent feature of a spiked bundle loaded core. Minimum shutdown margin is very sensitive to core designs. That said, what can be seen is the shutdown margin in the cell closest to the spiked bundle dropped by $\sim 1.3\%$ from 4% to 2.7%. While still having plenty of margin in this cell, it is well observed that loading these bundles has to be done carefully since they come in as very active fuel which could pose a safety concern if loaded into a limiting control cell. These bundles tend to behave in a fashion quite similar to traditional once-burned bundles; bundles that had gadolinium initially, but which has since burned out and now are more reactive fuel than when initially loaded.

In addition to a simulation utilizing the optimized lattice design, a comparison using a “base” lattice, which included Americium-241 loading but had not been processed through an optimization routine, was also performed. A comparison of the behavior of the optimized lattice in comparison to a non-optimized lattice was thus available; Figure 2.7 below shows these results.

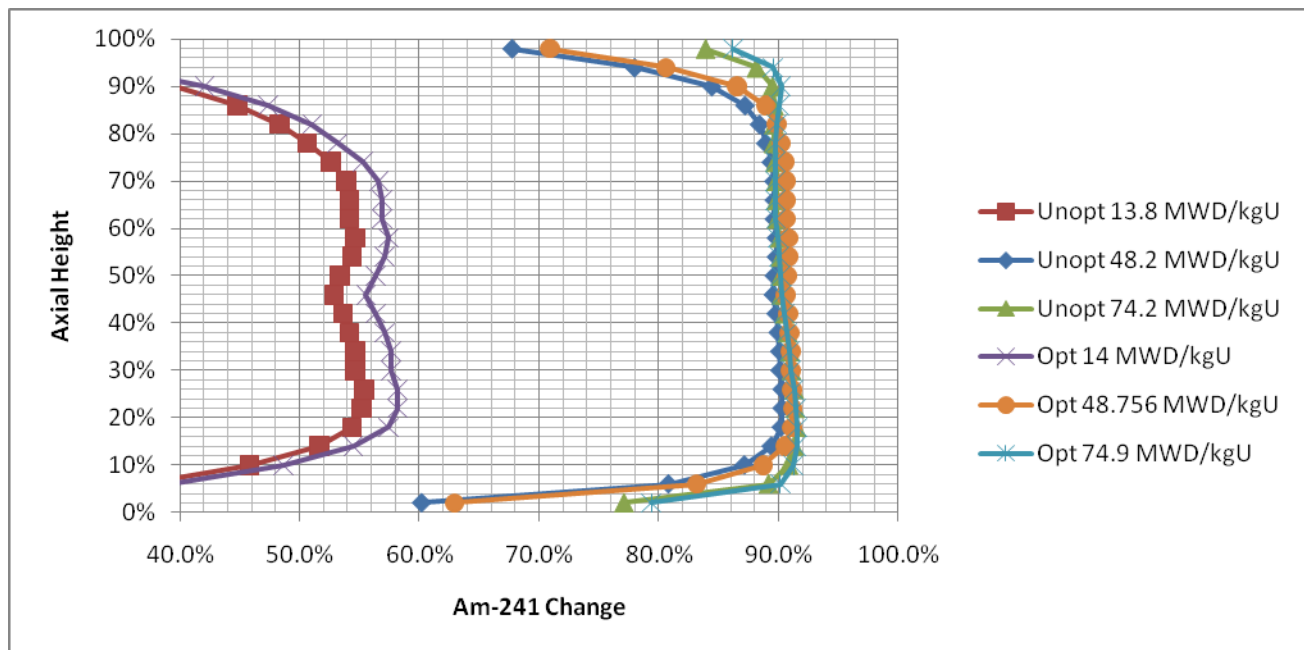


Figure 2.7 Axial Americium 241 Transmutation

Two items of particular interest are the variation (or lack thereof) when looking at axial transmutation dependencies and the transmutation results observed as burnup increases, as it pertains to the optimized and un-optimized lattices.

With respect to axial transmutation, the higher axial locations were thought to experience better transmutation rates due to the more advantageous absorption to capture ratios present in harder spectra. The results here show that the transmutation of Am-241 can be achieved in either the traditional thermal (axially lower) or harder spectrum (axially higher). One major limitation is that this only tracks overall inventory changes of Am-241 (production and losses included), but does not have the ability of tracking where exactly the Am-241 went. For example, did the Am-241 fission, or was it lost to higher actinides? The code employed, in fact, does not have the ability to track the full suite of actinides needed to address such question. That said, it is clear that Am-241 can be transmuted in a thermal spectrum and that there is not an obvious clear benefit of axial location in the BWR environment.

Also of interest are the transmutation results for the optimized and un-optimized bundles, as well as the trend with increasing burnup. At low burnup values, corresponding with once-burned fuel (~14 MWD/kgU), the optimized bundle showed a clear tendency to transmute the Americium 241 fuel faster than the non-optimized bundle, with approximately 5% greater transmutation than the un-optimized counterpart. This accelerated transmutation rate is not sustained throughout multiple cycles though, evidenced by the similar transmutation rates achieved at high burnups of ~50-75 MWD/kgU, where it appears a saturation point for americium-241 transmutation exists.

These proof-of-principle studies proved insightful and promising with regard to the potential of the effective transmutation of Am-241 in a BWR core. A major deficiency, however, is the inability to track the full suite of actinides; a capability needed to accurately evaluate if there is a clear advantage of the upper axial portions of a BWR core versus the lower, as well as needed to track if the americium isotopes are being incinerated through fission or simply transmuted into higher actinides that may still pose a radiological and storage hazards.

3. Two-Phase Thermal-Hydraulic Model

Thermal-Hydraulics Overview

In the conversion of NESTLE from a PWR modeling code to one that can also model a BWR core, the key need is that of a thermal hydraulic model capable of accurately capturing the boiling that occurs in each channel. Two boiling regimes are of primary interest in BWR channels, the section where sub-cooled boiling occurs and the section where saturated boiling occurs. Each of these two regimes needs to be modeled accurately in order to capture the correct moderator density, which has a strong impact upon core neutronics. Implemented into NESTLE, as part of this project, is a drift-flux scheme which has historically proven to be an accurate solution scheme in the steady state solution regimes, with relatively efficient code execution time. This scheme includes a model to capture sub-cooled boiling, and subsequently track when bulk boiling occurs. The determined flow conditions; both sub-cooled quality in the sub-cooled boiling regime and equilibrium quality in the saturated regime, are passed to a void-quality correlation to obtain the void fraction in each node, which is then used for the density calculation.

In addition to requiring a two-phase solution scheme, an accurate scheme for determining the correct flow inside each channel across the core is needed. The scheme employed inside NESTLE allows each user to choose to converge to a desired core pressure drop, or to converge to a total core mass flow rate. Once the user selects which option is desired and sets the appropriate target values, the code adjusts the flow inside each channel until the solution converges to within a user-defined tolerance, ensuring that there is an equal pressure drop across each channel, since the upper and lower plenums are common across all channels and each channel must then have the same inlet and outlet pressures.

The initial set of equations used include; the mixture continuity equation, mixture internal energy, and mixture momentum equations. These are illustrated by Equations 3.1-3.5.

Mixture continuity

$$A_x \frac{\partial \rho}{\partial t} + \frac{\partial}{\partial x} (G A_x) = 0$$

Equation 3.1

Mixture internal energy

$$A_x \frac{\partial}{\partial t} (\rho u) + \frac{\partial}{\partial x} (G u A_x) = -P \frac{\partial}{\partial x} \left(\frac{G}{\rho} A_x \right) + q'' A_x - P \frac{\partial}{\partial x} \left(\frac{\rho_l - \rho_g}{\rho} J_D^g A_x \right) - \frac{\partial}{\partial x} \left(\frac{\rho_l \rho_g}{\rho} (u_g - u_l) J_D^g A_x \right)$$

Equation 3.2

Mixture momentum

$$\frac{\partial}{\partial t} (\rho v) + \frac{1}{A_x} \frac{\partial}{\partial x} \left(\frac{G^2 A_x}{\rho} \right) = -\frac{\partial P}{\partial x} - \frac{\tau_w R_w}{A_x} - \frac{1}{A_x} \frac{\partial}{\partial x} \left(\frac{\rho_l \rho_g}{\rho} \left(\frac{1}{\alpha(1-\alpha)} \right) J_D^2 A_x \right) - \rho g \cos \theta$$

Equation 3.3

with

$$\frac{\tau_w R_w}{A_x} = f \left(\frac{G^2}{2 D_g \rho_l} \right) \phi_{frc}^2 + \sum_m \delta(x - x_m) K_m \left(\frac{G^2}{2 \rho_l} \right) \phi_{local}^2$$

Equation 3.4

and

$$\rho = \rho(u, P)$$

Equation 3.5

Finally, the relationship of the mixture quantities to the separate liquid and vapor phasic quantities are given by Equations 3.6-3.8.

$$v_g = + \frac{\rho_l J_D^g}{\rho \alpha}; \quad v_l = v - \frac{\rho_g J_D^g}{\rho (1-\alpha)}$$

Equation 3.6

$$v \equiv \frac{\rho v}{\rho} = \frac{G}{\rho} = \frac{(1-\alpha)\rho_l v_l + \alpha\rho_g v_g}{(1-\alpha)\rho_l + \alpha\rho_g}$$

Equation 3.7

$$\rho = (1-\alpha)\rho_l + \alpha\rho_g$$

Equation 3.8

Nestle Drift-Flux Solution

The drift-flux solution implemented uses a staggered mesh solution scheme so that thermodynamic properties are evaluated at node edges while the pressure is evaluated at node center; an illustration of the discretization of two nodes is shown below in Figure 3.1.

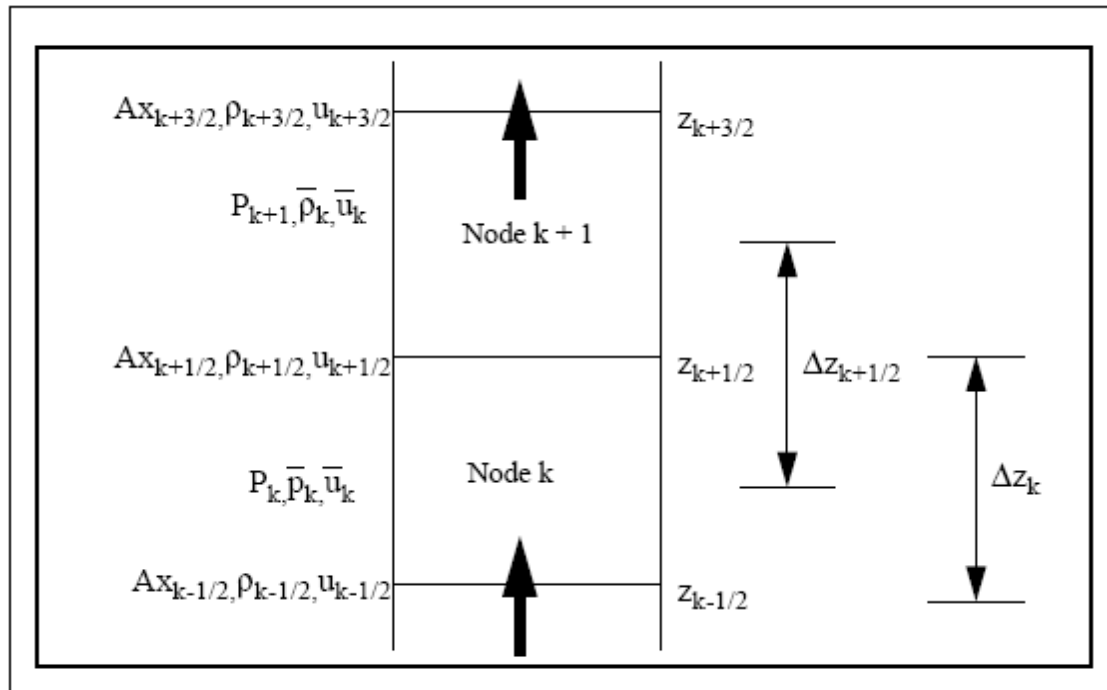


Figure 3.1 T-H Discretization

Using the discretized form of the equations, the first step involves solving the mass continuity equation up the channel.

Mixture Continuity

$$(GA_x)_{k+1/2} = (GA_x)_{k-1/2}$$

Equation 3.9

Next the internal energy equation is solved up the channel to allow for the determination of material thermal properties (density, temperature, quality, void fraction etc...).

Mixture Internal Energy

Once the internal energy distribution is known, it is then used to calculate the enthalpy distribution in order to determine the equilibrium quality up the channel. Subsequently, using the equilibrium quality distribution, the coolant temperature distribution is calculated; if equilibrium quality is less than 0, subcooled properties are used for temperature determination, alternatively if equilibrium quality is greater than 0, the temperature is set to the saturation temperature at the node pressure. Following the determination of temperature the true quality distribution up the channel is desired. In order to obtain an accurate estimate of true quality, determining the quality of net vapor generation (x_{nvg}) is necessary to account for subcooled boiling contributions. Two correlations are available as determinations of x_{nvg} , the Saha-Zuber model [23], which relates sub-cooled boiling to the surface heat flux and Peclet number, as well as an EPRI model developed by Lellouche and Zolotar [15] which contains a more complicated solution dependent on several flow parameters, material parameters as well as the heat flux; the EPRI model is the default model.

Saha-Zuber

If $Pe < 70,000$ then

$$x_{nvg} = \frac{-0.0022 * q'' * D_e * C_p}{k} \times \frac{1}{(h_v - h_l)}$$

Equation 3.10

If $Pe \geq 70,000$ then

$$x_{nvg} = \frac{-154 * q''}{G} \times \frac{1}{(h_v - h_l)}$$

Equation 3.11

Where:

q'' = Heat flux

D_e = Equivalent Diameter

C_p = Specific Heat Capacity

k = Thermal Conductivity

h_v, h_l = vapor enthalpy, liquid enthalpy

G = Mass Flux

EPR1

$$x_{nv}g = \frac{C_p * Z}{(h_v - h_f)}$$

Equation 3.12

$$Z = \frac{-B + \sqrt{B^2 - 4 * A * C}}{2A}$$

Equation 3.13

$$C = q'' * (4 * HB * q'' + HDB^2)$$

Equation 3.14

$$B = 2 * HDB^2 * (HHN + HDB/2) + 8 * q'' * HB * (HDB + HHN)$$

Equation 3.15

$$A = 4 * HB * (HDB + HHN)^2$$

Equation 3.16

$$HB = \frac{e^{(P/630)}}{0.072^2}$$

Equation 3.17

$$HDB = CDB * Ra^{0.8} * Pr^{0.4} * k / D_e$$

Equation 3.18

$$HHN = CHN * Ra^{0.666} * Pr * k / D_e$$

Equation 3.19

$$CHN = 0.2 * D_e / (4 * R_{rad})$$

Equation 3.20

$$CDB = 0.033 * s_{FRAC} + 0.013$$

Equation 3.21

$$x_{FRAC} = \frac{A_R}{(A_R + A_{rods})}$$

Equation 3.22

$$A_{rods} = N_{rod} * \pi * \frac{D^2}{4}$$

Equation 3.23

C_p = Specific Heat Capacity

h_{v,h_l} = vapor enthalpy, liquid enthalpy

q'' = Heat flux (BTU/hr-ft²)

P = Pressure (psia)

Re = Reynolds Number

Pr = Prandtl Number

k = Thermal Conductivity (BTU/hr-ft-°F)

D_e = Equivalent Diameter (ft)

R_{rod} = Heated Rod Radius

A_x = Cross-sectional Flow Area

N_{rod} = Number of fuel rods in bundle

D = Rod Diameter

Now that the qualities of net vapor generation, as well as the equilibrium (which will have negative values in the subcooled regime) are known, these two parameters are passed into a quality profile fit to determine true quality. There are several profile fits available, while the one implemented is one developed by Lahey and Moody [13] with a hyperbolic tangential fit:

$$x = \frac{(x_{eq} - x_{nvg} * (1 - \tanh(1 - x_{eq}/x_{nvg})))}{(1 - x_{nvg} * (1 - \tanh(1 - x_{eq}/x_{nvg})))}$$

Equation 3.24

Taking the newly determined true quality distribution, this is plugged into a void-quality correlation so that the void distribution can be determined and used to compute mixture density. Again, several options are available for void-quality correlations; available in NESTLE is the

Chexal-Lellouche model [2] , the Zuber-Findlay model [31] , and the Lellouche-Zolotar model [15] , which is the default option.

Lellouche-Zolotar

If $L_n \geq 0.2$

$$\alpha = \frac{A}{(1 + Y/x) * L_n}$$

Equation 3.25

If $L_n < 0.2$

$$\alpha = \sqrt{\frac{A}{(1 + Y/x) * C_1}}$$

Equation 3.26

$$Y = (1 - x) * \frac{\rho_v}{\rho_l} \left(1 + \frac{\rho_l * A * V_{gj}}{G * L_n (1 - x)} \right)$$

Equation 3.27

$$C_1 = L_n / A$$

Equation 3.28

$$V_{gj} = \left(\frac{1.41 * (\rho_l - \rho_v) * \sigma * g^2}{\rho_l^2} \right)^{1/4} * (1 - \alpha)^{3/4}$$

Equation 3.29

$$A = K_0 + (1 - K_0) * \alpha^r$$

Equation 3.30

$$r = \frac{(1 + 1.57 * \frac{\rho_v}{\rho_l})}{(1 - K_1)}$$

Equation 3.31

$$K_0 = K_1 + (1 - K_1) * \left(\frac{\rho_v}{\rho_l} \right)^{1/4}$$

Equation 3.32

$$K_1 = \min \left(\frac{0.8, 1}{1 + e^{-\left(\frac{Re}{150} \right)}} \right)$$

Equation 3.33

If $\alpha=0$

$$L_m = 1.0$$

Else

$$L_m = 1 - e^{-(C_1 \cdot \alpha)}$$

Equation 3.34

$$C_1 = 4 \cdot \frac{P_{crit}^2}{P \cdot (P_{crit} - P)}$$

Equation 3.35

x = quality

ρ_v, ρ_l = vapor density, liquid density

G = mass flux (lbm/hr-ft²)

σ = surface tension

g = gravitational constant

Re = Reynolds number

P_{crit} = Critical Pressure (psia)

P = Pressure (psia)

Upon inspection, it is noticed that this is an iterative solution for void fraction. The code must provide an initial guess for alpha, calculate the new alpha, compare the two and repeat until convergence is achieved.

Now that the void fraction is known, mixture density can be calculated and provided to the momentum equation solution. In addition, at this point it should be noted that both friction and form losses are needed in the solution of the momentum equation and a discussion of how friction losses and forms losses are calculated for two phase flow is needed. First a single phase friction factor term and similarly a single phase loss coefficient are determined. Subsequently,

after the single phase terms are known, a two phase multiplier is included to adjust the loss terms for two phase contributions:

$$\Delta P_{fric} = f \frac{G^2}{2D_g \rho_L} \phi_{fric}^2$$

Equation 3.36

Where f is the single phase Darcy-Wiesbach friction factor, and for normal BWR conditions takes the form:

$$f = 0.186 \cdot Re^{-0.2}$$

Equation 3.37

In addition, the two phase multiplier is calculated according to the Columbia correlation [21] .

$$\phi_{fric}^2 = 1 + x \left(\frac{\rho_L}{\rho_g} - 1 \right) \cdot C$$

Equation 3.38

If $P > 600$ psia

$$C = 1.02 \cdot x^{-0.17} \cdot G^{-0.48}$$

Equation 3.39

Else

$$C = 0.357 \left(1 + 10 \frac{P}{P_c} \right) x^{-0.17} G^{-0.48}$$

Equation 3.40

x = quality

ρ_v, ρ_L = vapor density, liquid density

G = mass flux (Mlbm/hr-ft²)

P_{crit} = Critical Pressure (psia)

P = Pressure (psia)

Similarly, local losses are a combination of a single phase loss term multiplied by a two phase loss coefficient:

$$\Delta F_{local} = K \frac{G^2}{2\rho_l} \phi_{local}^2$$

Equation 3.41

Where K is a user defined single phase local pressure loss coefficient for any component that may be an obstruction (spacer grids, lower orifice etc...). The two phase multiplier used is as computed as follows:

$$\phi_{local}^2 = 1 + E * x \left(\frac{\rho_l}{\rho_g} - 1 \right)$$

Equation 3.42

Where E is a constant again provided by the user to account for any non-homogenous two phase momentum loss. If E is set to 1.0 the equation reduces to the homogenous form of the two-phase loss multiplier and is the current default setting.

Finally the momentum equation is solved up the channel, using the properties determined from the internal energy equation and subsequent correlations, to obtain the pressure distribution. The new pressure distribution is then fed back into the internal energy equation to repeat the sequence. Again following the process described above, the new thermal properties are plugged into the momentum equation and the pressure distribution is again calculated. This process is iterated until a user defined convergence is achieved, where the pressure distribution and appropriate physical properties are then known. It should be noted that the internal energy equation and momentum equation are both solved in the drift-flux derived forms, given here in the momentum equation, and seen in the internal energy equation above.

Mixture Momentum

$$P_1(k+1) = P_1k - 1/(A_{fx})_1(k+1/2) [((GA_{fx})_1(k+1/2)^2)/(A_{fx}\rho^*)_1k - ((GA_{fx})_1(k-1/2)^2)/(A_{fx}\rho^*)_1k]$$

Equation 3.43

Flow Distribution

Another requirement for a robust thermal hydraulics scheme for the accurate solution of a Boiling Water Reactor during steady state operation is determining the correct flow rate to each of the fuel channels in the core. Since there is a common pressure shared by the upper plenum,

across all channels, as well as a common pressure shared across all channels in the lower plenum; there is a prescribed core ΔP , where each bundle is subject to have this same ΔP . Two options for solving for total core flow rate are often implemented in flow distribution models; solving for a user prescribed core ΔP , or solving for a user defined core mass flow rate; it should be noted that it is more common to solve for a total core mass flow rate. In NESTLE, solving for a core ΔP is just a subset of solving for a user defined core mass flow rate, such that creating a robust solver able to match a core ΔP by adjusting flow rates is a necessary first step for either of the solutions.

The method used for solving for a core ΔP , as well as solving for a total core flow rate, is taken directly from the FIBWR (Flow In A BWR) code manual [1] This code was developed in the early 1980's by EPRI and has a proven method for determining correct flow split details.

The solution process for solving for a core ΔP is as follows, on a channel by channel basis:

- (1) Guess flow rate for channel
- (2) Solve the drift flux set of equations to obtain a channel (and thus core) ΔP
 - a. If channel ΔP is within convergence criteria, the code is finished
 - b. Otherwise,
 - i. If ΔP is too low, increase flow rate in the channel
 - ii. If ΔP is too high, decrease flow rate in the channel
- (3) Go back to step (2) with new flow rates

Once each channel has achieved the necessary ΔP , the correct flow to each channel and all other necessary thermal hydraulic parameters (void fraction, density, internal energy, pressure etc...) are known, and the total core flow rate is computed by adding up the individual flow rates. Numerous schemes could be developed for determining the adjustment to the channel flow rate in the attempt to match ΔP ; the one chosen is derived from the FIBWR model and is given below:

After the 1st guess, projecting to the 2nd mass flow rate:

$$G_2 = G_1 \left(\frac{\Delta P_{1sg}^f}{\Delta P_1} \right)$$

Equation 3.44

After the 2nd calculation, projection to the 3rd mass flow rate:

$$G_3 = G_1 - (G_1 - G_2) \left(\frac{\Delta P_1 - \Delta P_{1sg}^f}{\Delta P_1 - \Delta P_2} \right)$$

Equation 3.45

Following the 3rd calculation, from henceforth a polynomial extrapolation of the three most recent sets of G and ΔP is used to project to the nth mass flow rate:

$$G_n = A + B \Delta P_{1sg}^f + C (\Delta P_{1sg}^f)^2$$

Equation 3.46

$$C = \left[\frac{(G_{n-2} - G_{n-1})}{(\Delta P_{n-2} - \Delta P_{n-1})} - \frac{(G_{n-2} - G_n)}{(\Delta P_{n-2} - \Delta P_n)} \right] / (\Delta P_{n-2} - \Delta P_n)$$

Equation 3.47

$$B = \frac{(G_{n-2} - G_{n-1})}{(\Delta P_{n-2} - \Delta P_{n-1})} - C (\Delta P_{n-2} + \Delta P_{n-1})$$

Equation 3.48

$$A = G_{n-2} - B \Delta P_{n-2} - C (\Delta P_{n-2})^2$$

Equation 3.49

Typically, convergence on the order of 1E-5 is met in less than 10 iterations, and much of the time convergence is achieved in 3-4 iterations. Occasionally, when there are several flow and pressure drop combinations that are very close to the solution, the polynomial extrapolation will provide an anomalous projection. To protect against this, a maximum and minimum flow rate/ΔP combination is kept track of and if a solution is provided that is outside of this maximum or minimum a linear interpolation is used to project the new flow rate and the code continues as usual. In addition, occasionally two subsequent solutions will yield a ΔP identical to the previous, or two previous, solutions which causes a divide by 0 and the code crashes due to a

segmentation fault. Several checks have been instituted in the code that catch these errors as well as similar errors, and subsequently coax the code back into a convergent solution.

In the case of converging to a total core flow rate, the code uses the ΔP solver as a subset of the solution process, which goes as follows:

- (1) Guess an initial core ΔP
- (2) Move to core ΔP solver described above
- (3) Once each channel is solved to the core ΔP , add up the individual channel flow rates
 - a. If core flow rate is within convergence criteria, the code is finished
 - b. Otherwise,
 - i. If core flow rate is too low, increase the ΔP guess
 - ii. If core flow rate is too high, decrease the ΔP guess
- (4) Go back to step (2) with updated core ΔP

In a scenario very similar to predicting what the next guess for channel flow rate should be, the same type of a solution process for predicting the core ΔP has been implemented.

After the 1st guess, projecting to the 2nd ΔP :

$$\Delta P_2 = \Delta P_1 \left(\frac{G_{core}}{G_1} \right)$$

Equation 3.50

After the 2nd calculation, projection to the 3rd ΔP :

$$\Delta P_3 = \Delta P_1 - (\Delta P_1 - \Delta P_2) \left(\frac{G_1 - G_{core}}{G_1 - G_2} \right)$$

Equation 3.51

Following the 3rd calculation, from henceforth a polynomial extrapolation of the three most recent sets of G and ΔP is used to project to the n^{th} ΔP :

$$\Delta P_n = A + B G_{core} + C (G_{core})^2$$

Equation 3.52

$$C = \left[\frac{(\Delta P_{n-2} - \Delta P_{n-1})}{(G_{n-2} - G_{n-1})} - \frac{(\Delta P_{n-2} - \Delta P_n)}{(G_{n-2} - G_n)} \right] / (G_{n-2} - G_n)$$

Equation 3.53

$$B = \frac{(\Delta P_{n-2} - \Delta P_{n-1})}{(G_{n-2} - G_{n-1})} - C(G_{n-2} + G_{n-1})$$

Equation 3.54

$$A = \Delta P_{n-2} - B G_{n-2} - C(G_{n-2})^2$$

Equation 3.55

The sample size for this is much smaller in a core simulation than the solution for pressure drop, since the ΔP solver may solve hundreds of channels for every single iteration on core flow rate. That said, it has been seen that usually no more than 5-6 iterations on core ΔP is required to achieve total mass flow rates within a convergence on the order of 1E-5.

Thermal Limits

Part of the ongoing work will ultimately connect the simulator results of relative power distributions and two-phase flow conditions to a reasonable assessment of core thermal limits. Typical assessments that will be sought will be the evaluation of the critical power ration (CPR) and assessments related to linear power density (kw/ft) generation in each bundle. Currently, these assessments can be indirectly inferred via reasonable expectations in radial and axial relative power distributions.

4. Code Validation

Thermal-Hydraulic Validation

Benchmark Overview

Upon completion of the thermal hydraulic drift-flux solution scheme, of which a detailed description is provided in Chapter 3, a benchmark to serve as a check for the validity of the programming as well as the accuracy of the solution was performed. The benchmark used for this is the “OECD/NRC Benchmark Based on NUPEC BWR Full-Size Fine-Mesh Bundle Tests (BFBT)” [1]. The benchmark was conducted in two parts. First a benchmark of the hydraulics is performed, where single phase flow is passed through an 8x8 bundle without power. With a detailed description of the bundle design provided, the various required hydraulic parameters were able to be retrieved (equivalent diameter, heated diameter etc...), in addition locations of spacer grids as well as corresponding loss coefficients were provided. This allowed for an assessment of the accuracy in predicting pressure across a channel as water flows, prior to assessing the validity of the calculated void fraction. The second part of the benchmark consists of benchmarking the void fraction calculation against the measured values provided in the experiment, where the channel was supplied various power profiles. Thus this allows for an understanding of the accuracy when using the subcooled quality correlation (EPRI model or Saha-Zuber) as well as the void-quality correlation (Lellouche-Zolotar).

Experiment Description

The fuel bundle used for experimental analysis was composed of the data provided in the following Table 4.1.

Table 4.1 Benchmark Bundle Specifications

Parameter			
C2A			
Array -x,y	8 x 8	Water rod O.D. (in)	1.34
Nrods	60	Water rod Radius (in)	0.67
Pitch (in)	0.64	Fuel Rod Area (in**2)	12.46
Heated length (in)	145.98	Bundle Total Area (in**2)	27.13
Channel Inside dimensions -x,y	5.22	Ax (in**2)	14.67
Channel Inside dimensions -y	5.22	P-Wet (in)	115.81
Inside Corner Radius	0.31	P-heated (in)	91.28
Fuel Rod O.D. (in)	0.48	De (4*Ax/PW) (in)	0.51
Fuel Rod Radius (in)	0.24	Dheat (in)	0.64

The entire length of heated fuel was the same lattice, an 8x8 bundle with the four center rods being replaced by one large water rod. In the bundle 7 spacers were present, centered at axial locations 15.4, 3.22, 4.90, 6.58, 8.26, 9.94, and 11.62 feet. Each spacer was identical and was reported to each have a loss coefficient of 1.2, although there is a discrepancy regarding this that will be discussed later. For the single phase experiments, five different test cases were performed for the hydraulic test, P70027, P70028, P70034, P70035, and P70036. Each case had different inlet conditions, which are given in Table 4.2 below:

Table 4.2 Single Phase Experiment Initial Conditions

	Outlet Pressure		Inlet Temp		Flow Rate		Bundle Delta P		Inlet Pressure
	MPa	psia	°C	°F	ton/hr	lbm/hr	(kPa)	psia	
P70027	7.15	1037.02	284.9	544.82	20.3	4.475E+04	3.12	0.453	1037.47
P70028	7.16	1038.47	285.1	545.18	24.9	5.490E+04	4.59	0.666	1039.14
P70034	7.15	1037.02	284.8	544.64	59.7	1.316E+05	23.87	3.462	1040.48
P70035	7.16	1038.47	284.6	544.28	64.8	1.429E+05	27.77	4.028	1042.50
P70036	7.15	1037.02	284.8	544.64	69.9	1.541E+05	32.03	4.646	1041.67

Single Phase Results

The first benchmark consists of testing the hydraulic part of the drift-flux solution. While this does not help to assess the accuracy of the sub-cooled boiling and void quality correlations, this does serve to assess the accuracy of the staggered mesh scheme, going from the continuity

equation, through the internal energy equation and through the momentum equation. Practically, this can also help discern how much error may be due to the hydraulic solution when using the powered experiments.

From the five experiments listed in Table 4.2, the data associated with “Bundle Delta P” correlates with the total bundle pressure drop over the active test length and is one metric for the assessment of the accuracy of the drift-flux solver. This “Bundle Delta P” is represented by pressure tap “dp309” in the experimental data. In addition, several additional pressure tap locations were also recorded and used as benchmark experiments. One item that is important to note is that the total pressure drop over the ~146 inches is reported with the static pressure head subtracted out, so as to give a more detailed result of pressure loss mechanisms due to friction and forms losses. The first two results (Figure 4.1 and Figure 4.2) given below show the relative error generated with the use of three different spacer loss coefficient values for the two lower flow experiments.

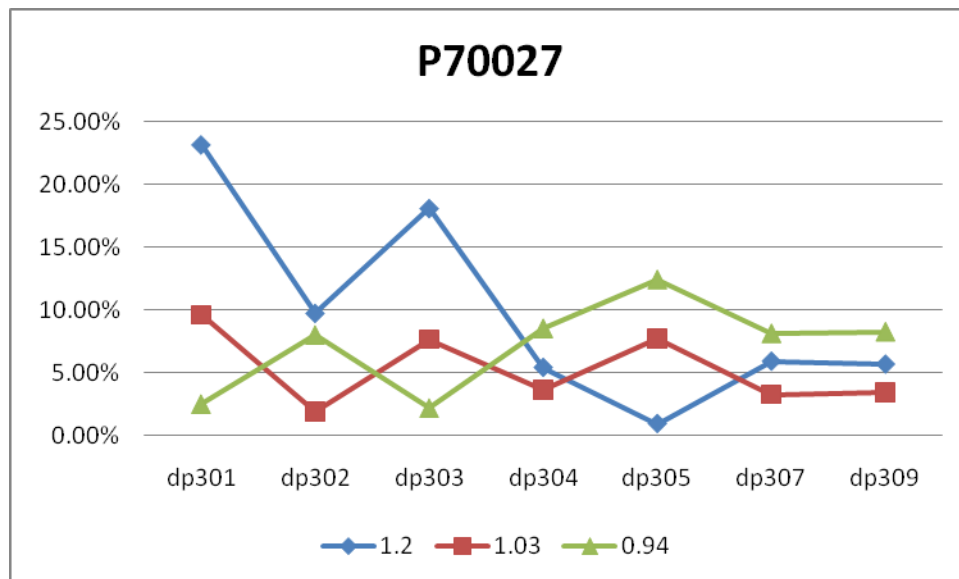


Figure 4.1 Single Phase Pressure Drop

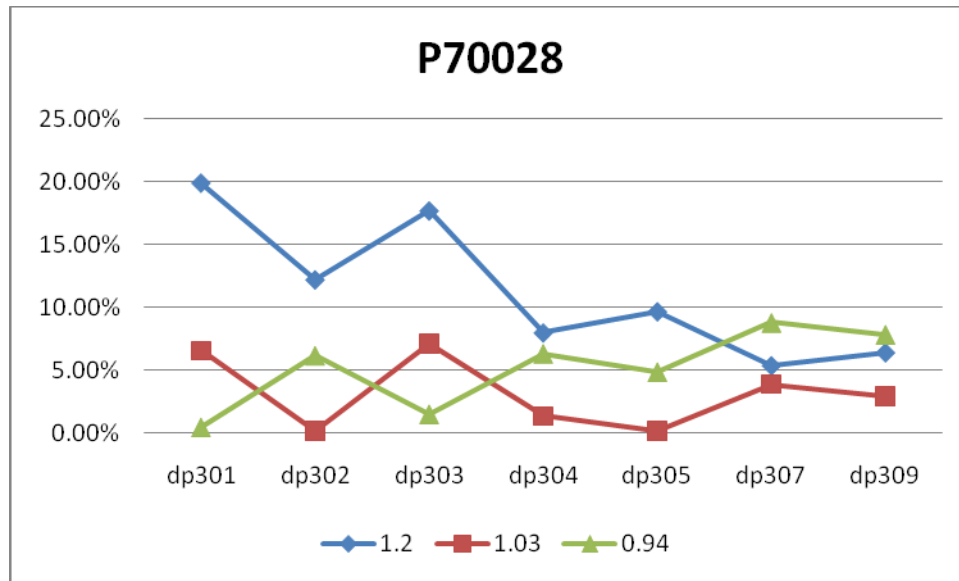


Figure 4.2 Single Phase Pressure Drop

The following three charts (Figure 4.3, Figure 4.4 and Figure 4.5) show the relative error using the various loss coefficients for the three high flow cases. A discussion of the derivation and applicability of the loss coefficients will follow, as the accuracy of the solution depends strongly on the spacer loss coefficient. Observed is the trend of the error according to the recommended 1.2 loss coefficient growing as the flow rate increases, as well as the clear observation that a loss coefficient of 1.2 leads to an overestimate of the pressure drop. Regarding the large errors observed at pressure taps dp301 and dp303; the outlet sensors for these two pressure drop measurements lie immediately after a spacer grid. Since the primary mechanism for pressure drop for these two measurements is heavily weighted towards the local losses, since very little friction losses have occurred as the locations are near the beginning of the active length, the spacer loss coefficient will be the primary driver for pressure loss at these locations.

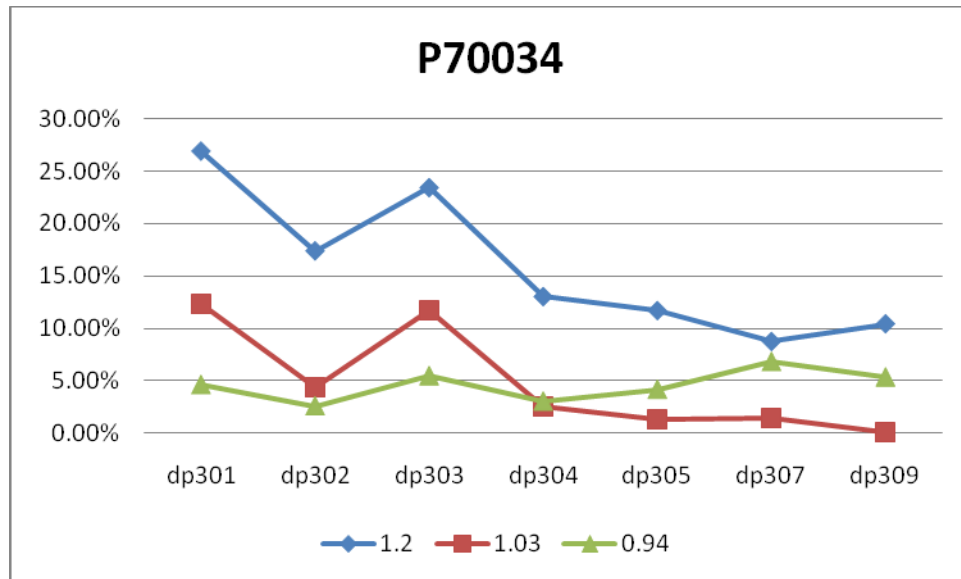


Figure 4.3 Single Phase Pressure Drop

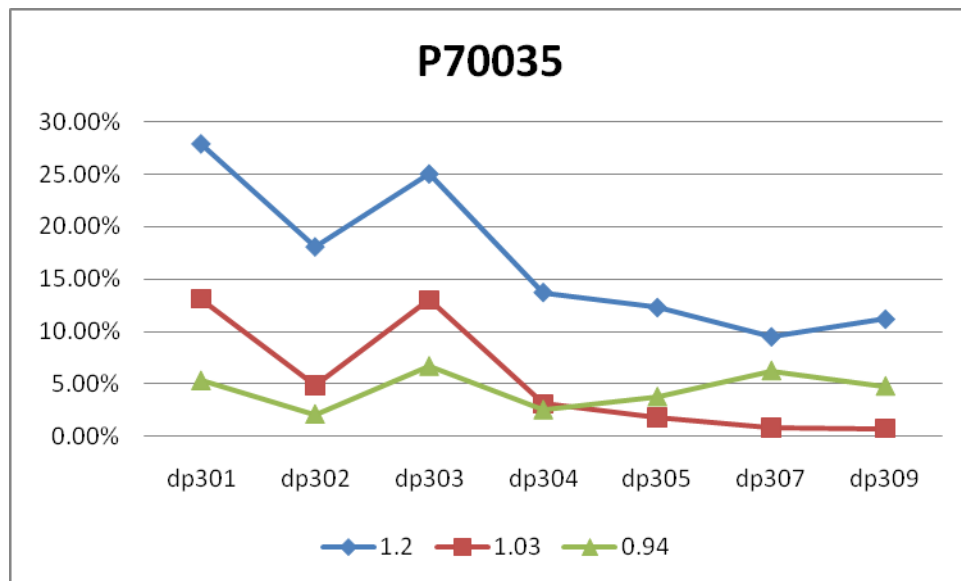


Figure 4.4 Single Phase Pressure Drop

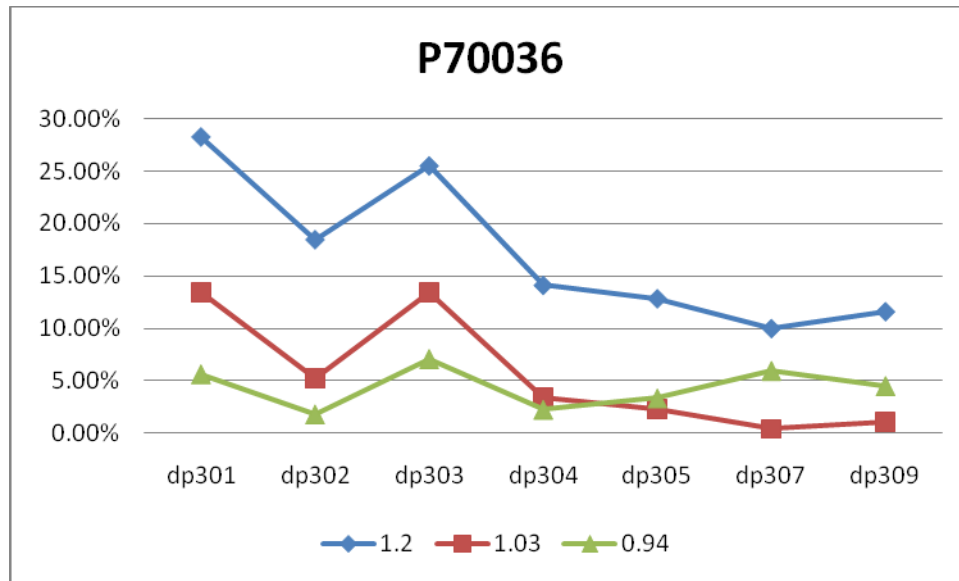


Figure 4.5 Single Phase Pressure Drop

Due to this consistent overshoot according to the recommended spacer loss coefficient, the coefficient was then adjusted in an attempt to more closely match the experimental results. After a sensitivity study of numerous loss coefficients was performed, a loss coefficient of 1.03 was determined to yield very accurate answers, where this loss coefficient dropped the relative error in every case, and found extremely good agreement for the cases with higher pressure drops. The results are shown here in tables 1.6. through 1.8.

Furthermore, a discussion of the loss coefficient was treated in detail by Gluck in reference [9]. Here, a mechanism for calculating sub-channel loss coefficient is introduced, based on the method by Shiralakar and Radcliffe (1971) [24]. These sub-channel loss coefficients are then weighted by the cross-sectional area occupied by each sub-channel to obtain an estimated average bundle loss coefficient via the parallel resistance method. Concurrently, experimentally derived results for the estimated bundle loss coefficient are used to compute a scaling factor that is then used to scale the computationally derived loss coefficient according to the scaling factor. Using this method, an average loss coefficient of 0.94 was determined and thus used as the third benchmark loss coefficient seen in the results. It should be mentioned that in this report there were some doubts about the fidelity of the quoted 1.2 loss coefficient in the original experiment,

noting that the results obtained using 1.2 were all overshooting the pressure drop estimates, which is similar to what was seen using the drift-flux model with a loss coefficient of 1.2. In addition, it is pointed out that the same loss coefficient was used for a geometrically different space grid. According to Gluck [9]

“In the BFBT benchmark specification (Neykov et al., 2006) a constant bundle loss coefficient of 1.2 is given (remarkably the same value as for the geometrically quite different lantern type spacer grid). However, calculations based on this value lead to strong over estimations in pressure loss; whereas calculations with the above derived loss coefficients [0.94 bundle average] yield very good results.”

Given the uncertainty in the space loss coefficient, with quoted values ranging from 1.2 to 0.94, the calculated results show good agreement with experimental results. The worst agreement occurred at a loss coefficient of 1.2, and high flow conditions, resulting in errors on the order of 11% and a low error of 6% on the low flow conditions. On the flip side, when using a loss coefficient of 0.94, the high error occurred at low flow conditions and corresponded to an error of ~8% while the low error occurred at the high flow conditions and pertained to an error of ~4%. In addition, the computed pressure drop profile up the channel was also observed to follow the same trend of the experimental results at both low flow conditions (experiment P70027) and high flow conditions (experiment P70036), as seen in the relative error pertaining to the intermediate pressure taps. Unfortunately, no error analysis was found regarding to reliability of each loss coefficient to determine if the loss coefficient of 1.03 is within, or near the error boundaries. In any event, the flow conditions typical of a BWR core are much closer to the high flow condition, represented by test case P70036, which when using a recommended loss coefficient of 0.94 gives a relative bundle pressure drop error of 4.5%.

Two-Phase Results

While benchmarking the drift-flux solver against single-phase pressure drop measurements serves beneficial to ensure correct coding, the intention of the code is to accurately model two-phase flow primarily to calculate the void fraction in each node, in order then in turn calculate

the moderator density to finally obtain the correct homogenized cross-sections. The benchmark experiment had a large matrix of available data, with numerous degrees of freedom. The outlet quality varying from 2% to 25%, various flow rates, various operating pressures, as well as multiple axial power profiles. Due to this, two axial power profiles were chosen; a case with uniform heating as well as a bottom peaked power profile, which is representative of the power profile for BWRs at operating conditions. For each of these two power profiles, four test cases were used for a comparison of void fraction yielding eight test cases, where the initial conditions for these cases are given below in Table 4.3.

Table 4.3 Two Phase Experiment Initial Conditions

	<i>Inlet Pressure</i>		<i>Inlet Temp</i>		<i>Flow Rate</i>		<i>Power</i>	
	MPA	psia	C	F	TON/HR	LB/HR	MW	BTU/hr
0011-53	7.21	1046	278.6	533.5	54.47	1.20E+05	1.24	4.23E+06
0011-55	7.21	1046	278.5	533.3	54.03	1.19E+05	1.9	6.48E+06
0011-57	7.19	1043	278.6	533.5	54.84	1.21E+05	2.59	8.84E+06
0011-59	7.24	1050	277.9	532.2	54.96	1.21E+05	4.87	1.66E+07
0011-61	7.28	1056	277.9	532.2	54.79	1.21E+05	6.44	2.20E+07

	<i>Inlet Pressure</i>		<i>Inlet Temp</i>		<i>Flow Rate</i>		<i>Power</i>	
	MPA	psia	C	F	TON/HR	LB/HR	MW	BTU/hr
0031-15	7.21	1046	278.4	533.1	54.97	1.21E+05	1.23	4.20E+06
0031-16	7.22	1047	278.4	533.1	55	1.21E+05	1.92	6.55E+06
0031-18	7.23	1049	278.4	533.1	54.79	1.21E+05	3.52	1.20E+07
0031-20	7.22	1047	278.1	532.6	54.83	1.21E+05	4.86	1.66E+07
0031-21	7.25	1052	275.5	527.9	54.9	1.21E+05	6.45	2.20E+07

The experimental mechanism for determining the outlet void fraction is composed of taking high resolution pictures, in these cases using a CT scanner, and using software to compute the volume occupied by the vapor phase as well as the liquid phase in each axial slice [18] . Using this method and the initial conditions given above, the measured outlet void fraction is provided

below along with the calculated void fraction and relative error induced by using the drift-flux model in Table 4.4.

Table 4.4 Two Phase Benchmark Results

	Void Fraction				
	0011-53	0011-55	0011-57	0011-59	0011-61
Experimental:	19.9%	40.9%	53.5%	72.6%	79.4%
Calculated:	27.1%	45.7%	56.9%	74.0%	80.1%
Relative Error:	36.4%	11.8%	6.4%	1.9%	0.9%
	0031-15	0031-16	0031-18	0031-20	0031-21
Experimental:	20.1%	39.3%	62.3%	71.5%	78.3%
Calculated:	25.8%	45.1%	65.9%	74.2%	79.6%
Relative Error:	28.3%	14.8%	5.8%	3.8%	1.7%

Of particular interest is the decrease in error as the void fraction increases, hence errors on the order of 30% are present at low void fractions of ~20%, yet the error when increasing above 70% shrinks to be on the order of ~1-2%. Practically, this result is beneficial as the most reactive fuel bundles in the core will experience void fraction values greater than 70%, rather closer to 80%, where the drift-flux model produces the most accurate results. In addition, the quoted error for the void fraction measurement test was 2%, thus the two very high void cases nearing 80% are both within the error of the experimental results. The following Figure 4.6 shows a graphical representation of the error that would be induced into a density calculation as a result of the error in void fraction, as well as the accuracy potential when taking the 2% error into account and propagating this through to the density calculation, using data at 1045 psia and 550 °F which is very representative of BWR operating conditions. Thus if the calculated error was found to be below the error range for the density calculation, the relative error is set to 0% since the calculated result was within the prescribed tolerance. This is an important assessment since the void fraction calculation is performed for the primary purpose of determining the correct moderator (water) density in order to obtain the correct macroscopic cross-sections.

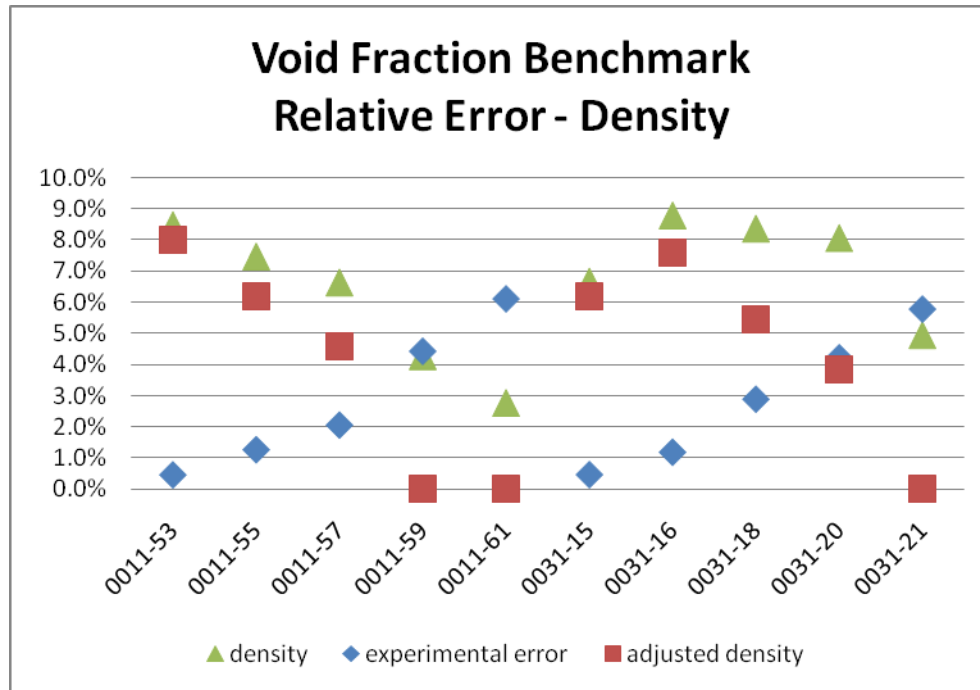


Figure 4.6 Two Phase Benchmark Density Results

Notice the change in the magnitude of the error for the low void fraction experiments, 0011-53 and 0031-15. Errors that were on the order of 30% in void fraction shrunk to less than 10% in moderator density. To further quantify the effect that the error in void fraction will ultimately have on core neutronics, which is the primary purpose in calculating void fraction, lattice physics simulations were performed for three of the experiments. Using three representative state points from the previous suite of comparisons, k_{∞} was calculated at the experimental void fraction as well as at the calculated void fractions. This data was then used to assess the error introduced in the core neutronics since k_{∞} serves as a sort of “catch all” for important neutronics parameters affected by void fraction. Experimental and calculated results for experiments 0011-53, 0011-55 and 0031-20 were used, where the simulations were performed with burnup extending out to 45,000 MWD/MTU to investigate any possible propagated error, with the results given below in Figure 4.7.

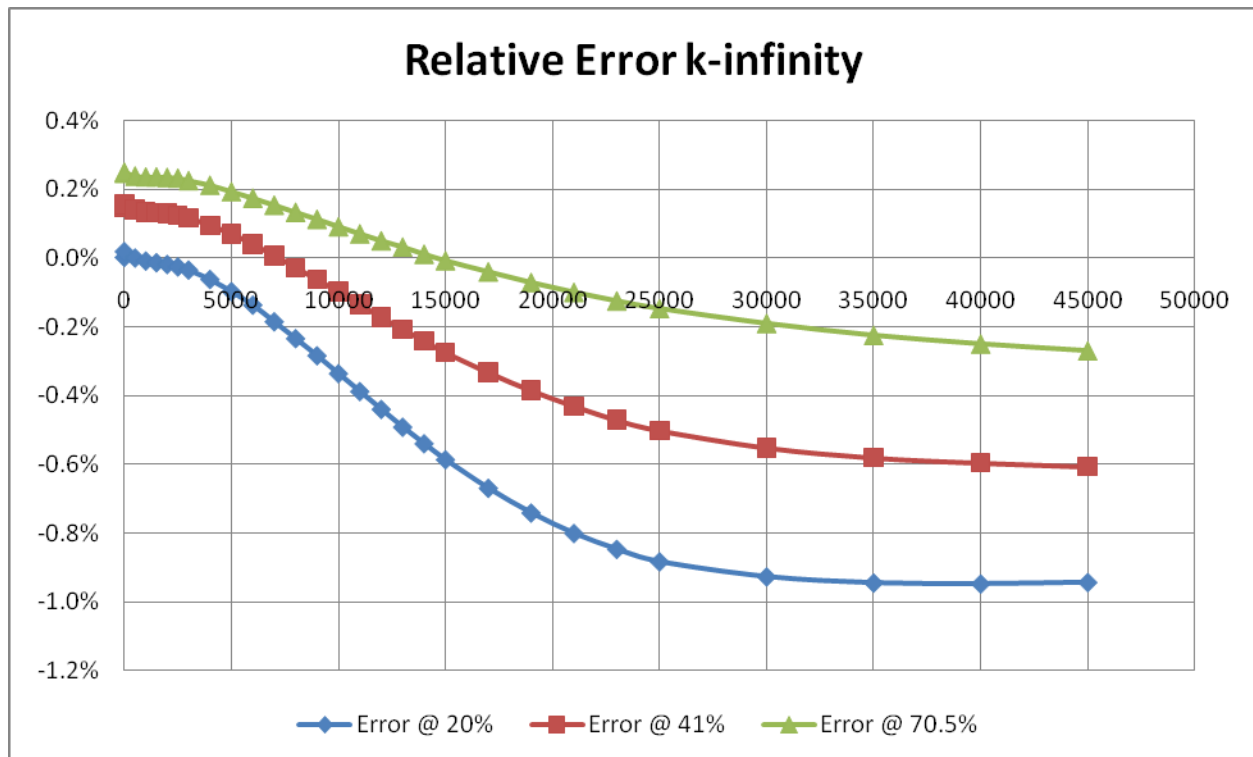


Figure 4.7 Two Phase Benchmark Void Fraction Propagated Error

At low burnups, typical of bundles in once-burned state, the error for all three bundles is low, and actually decreases for two of the cases during the early burnup. Following this early behavior, all three tend to increase slowly and move towards an under-estimate of reactivity due to the overestimate of void fraction. All appear to trend towards an equilibrium error, with the lowest error pertaining to the highest voids.

While it would be advantageous to not just check the accuracy of the outlet void fraction, but to also profile the axial void fraction error, but unfortunately the data available provided only an outlet void fraction and this was not an option. Practically, when coupling the thermal-hydraulic solver to the full 3-D core simulator and benchmarking against known core configurations and core loading patterns, an implicit benchmark will be performed; albeit a benchmark that has multitudes of sources of error above just the thermal-hydraulic solution.

Coupled Neutronics and Thermal Hydraulics Validation

Peach Bottom Benchmark Description

Upon the completion of the drift-flux mode, as well as the flow redistribution model the big question of “is it accurate” exists. The benchmark chosen for the coupled neutronics and thermal-hydraulics test was an EPRI report regarding the Peach Bottom Cycle 1 core [14]. This cycle is somewhat of an anomaly of a core with respect to the control blade movements and power changes, when compared against modern core designs, but with the vast publicly available operating data, as well as TIP (travelling in-core probe) data it serves as an excellent reference. In addition, the various power changes and flow changes, this allows for the benchmarking over a wider range of thermal-hydraulic conditions.

Peach Bottom Cycle 1 is a large 764 bundle core, with a rated power of 3293 MW and a rated power of 102.5 Mlbm/hr and 185 control rods. Inlet pressure is estimated to be 1050 psia, with the inlet enthalpy being 521.3 btu/lbm. The core loading pattern, contrary to modern loading patterns, is not symmetric in any dimension, half-core, quarter-core; neither mirrored nor rotational. Three different bundle types are present in the core. Bundle type 1 is enriched to 1.10% in U-235 and has no gadolinium rods present, bundle type 2 is enriched to 2.50% with 4 gadolinium loaded rods, lastly bundle type 3 is also enriched to 2.50% with 5 gadolinium loaded rods. The cycle 1 core loading pattern, with respect to bundle type, is given here as Figure 4.8.

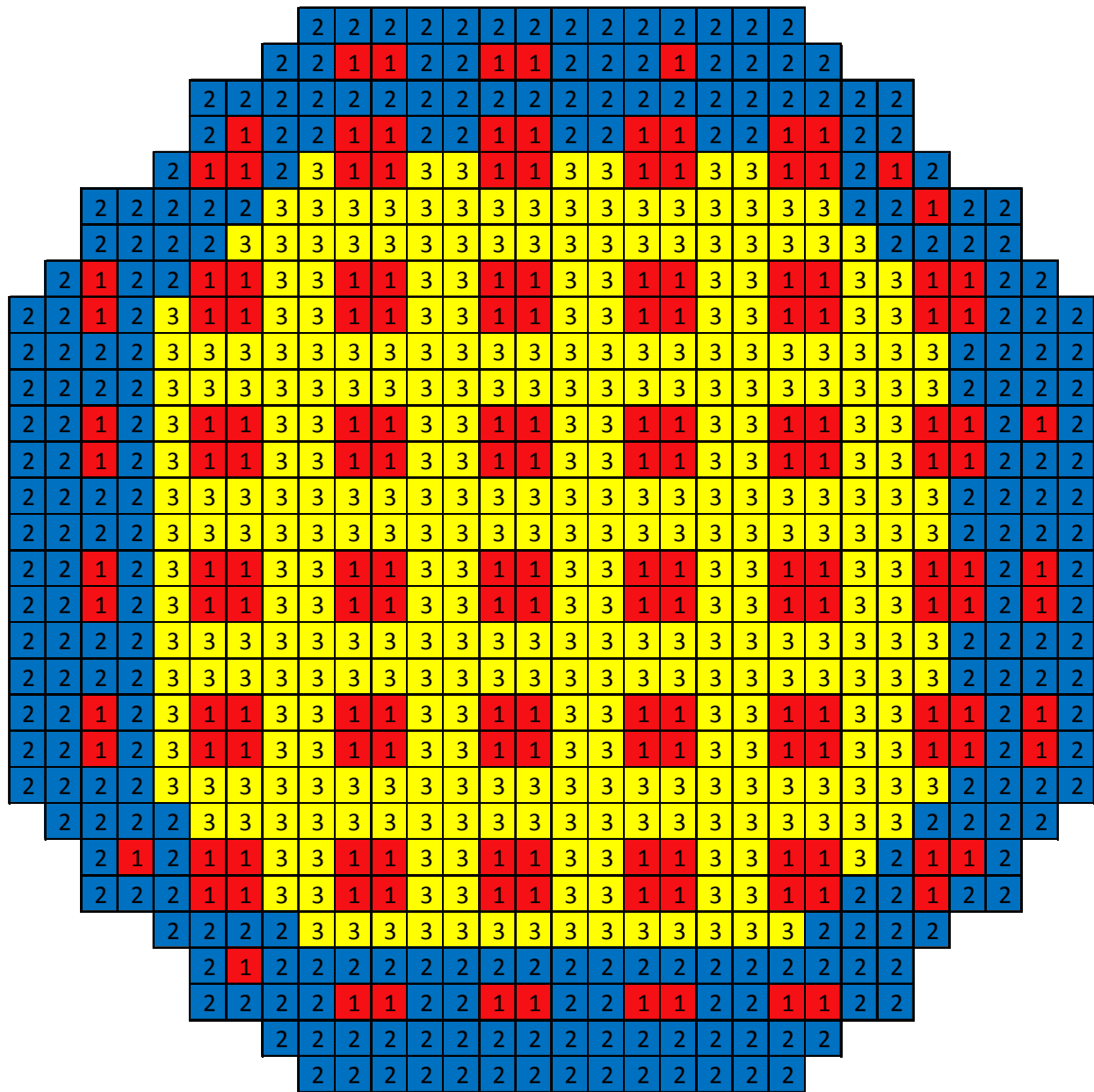


Figure 4.8 Peach Bottom Cycle 1 Core Loading Pattern

The state point dependent parameters required for input throughout the cycle (excluding rod patterns) are given below in Table 4.5.

Table 4.5 Cycle 1 Operating Conditions

Avg. Exposure	Core Power	Core Flow	Bypass Flow
MWD/MTU	% Rated	% Rated	Mlb/hr
230	55.7%	103.3%	13.64
390	79.0%	105.3%	13.94
648	76.3%	70.3%	8.47
741	96.1%	105.1%	13.91
1010	99.0%	103.0%	13.59
1585	99.6%	94.7%	12.29
2080	100.0%	100.6%	13.21
2555	99.1%	98.7%	12.92
2920	86.7%	76.8%	9.48
3542	99.3%	101.3%	13.32
4364	99.6%	101.6%	13.36
4697	99.5%	101.5%	13.35
5262	100.0%	100.6%	13.21
5640	99.7%	103.5%	13.67
6106	97.6%	103.5%	13.67
6470	96.3%	102.8%	13.56
7000	50.1%	48.9%	5.10
7300	56.3%	38.9%	3.54
7712	57.2%	39.4%	3.61
8100	56.4%	39.9%	1.89
8430	99.8%	104.5%	6.81
8766	100.0%	98.7%	6.37
9295	98.8%	104.1%	6.78
10100	91.1%	105.8%	6.91

Cycle 1 rod patterns at each statepoint are included in the report, but only the initial rod pattern will be listed below in Figure 4.9; if further rod patterns are needed the aforementioned EPRI report contains the full listing. The numbers given indicate the number of notches inserted (from the bottom), where each notch is 3 inches. Also, in BWR cores, the control blade occupies four fuel bundle locations, thus for each control rod location below, four fuel bundles are within the control cell, with the nomenclature referencing the top left bundle.

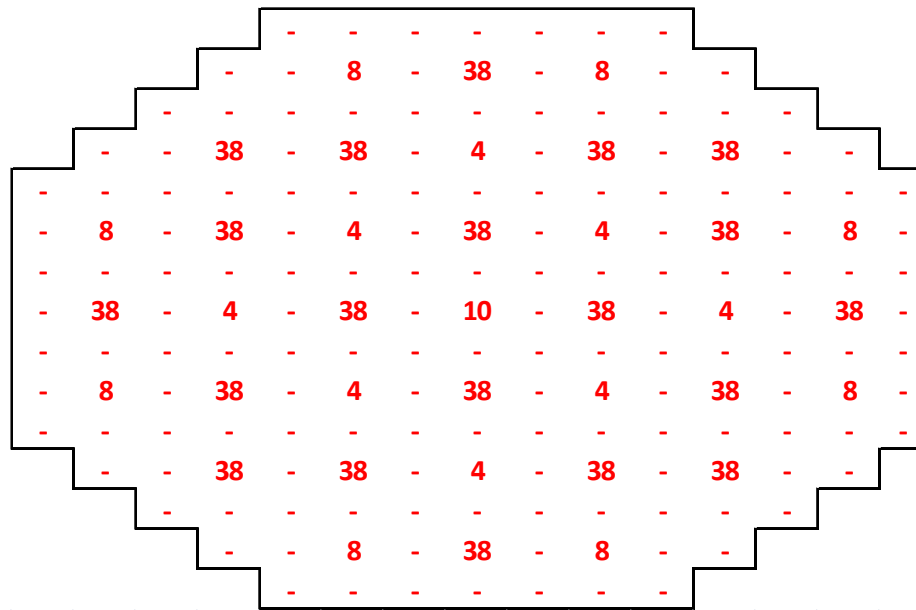


Figure 4.9 BOC Control Rod Pattern

In reference to core flow rate specification, bypass flow rate is an important parameter in BWR cores and needs some clarification. Since BWR bundles are canned, there are two flow rates of importance; the flow in-bundle and the flow outside of the bundles, and it is this outside flow that is called the bypass flow. In modern core designs there are also water rods designed in the bundle to increase moderation, and there appears to be no consensus if bypass flow does or does not include water rod flow. In NESTLE, the bypass flow represents the total flow outside the bundles, as well as the flow inside the water rods and should be computed and input as such. For Peach Bottom Cycle 1, none of the bundles were designed with water rods present so it is a moot point, but since NESTLE is capable of modeling modern reactor designs as well this should be mentioned to avoid confusion.

In a BWR flow profiling is accomplished via designing inlets and tie plates to control the pressure drop across each channel via local losses at these components. Since two-phase pressure losses are greater than single phase pressure losses, the natural inclination is for the flow to divert away from the hot channels, to the lower power channels which are typically located on the periphery. To help redistribute this flow to the orifice used on the peripheral bundles is

typically much greater than the orifices for the internal bundles. In addition, different lower tie plate designs may be used to divert flow to, or away from, certain bundles. The following Figure 4.10, gives the orifice and lower tie plate specifications for peach bottom cycle 1.

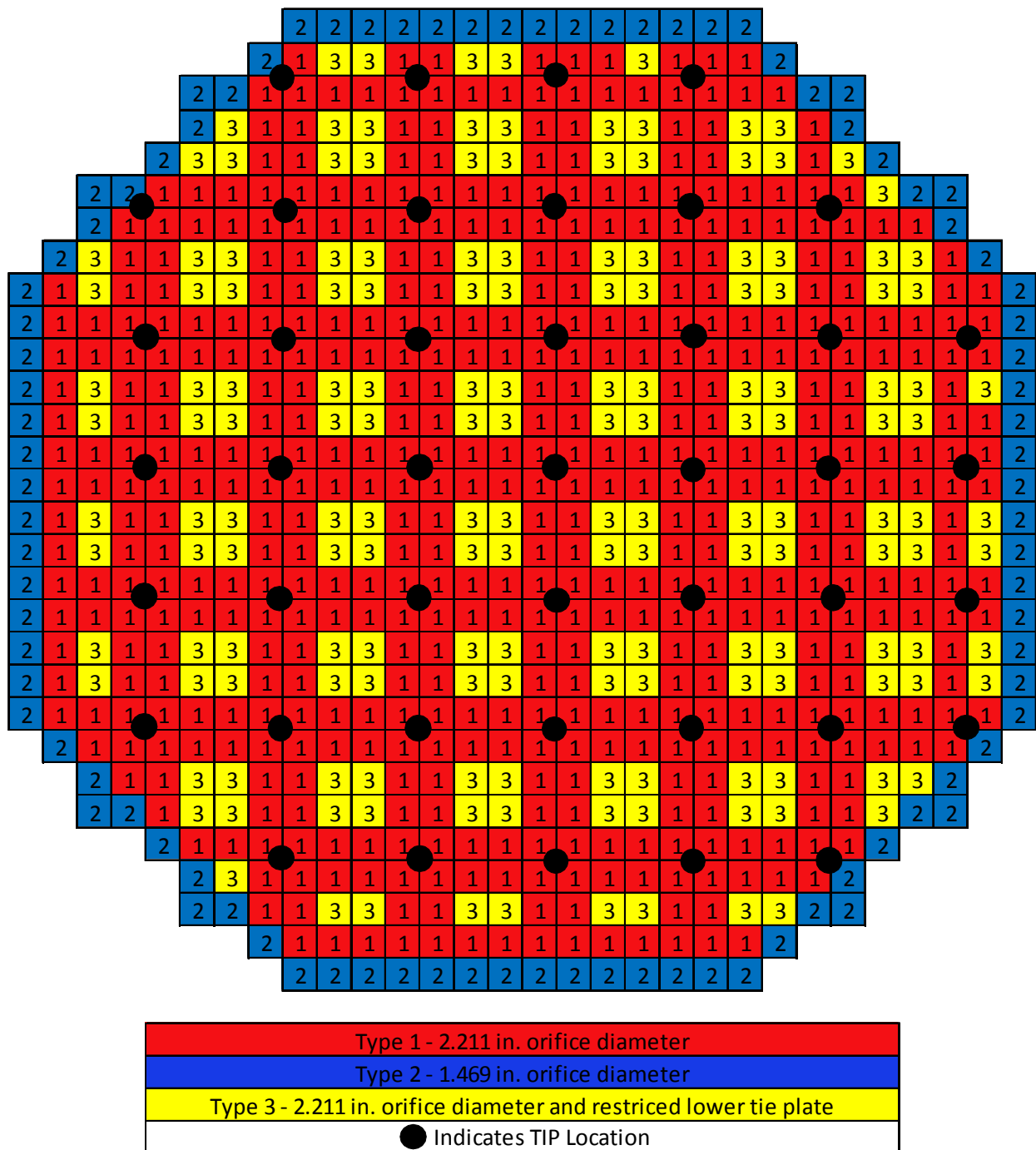


Figure 4.10 Peach Bottom Cycle 1 Orifice and TIP Locations

Lastly, both axial and radial reflectors were added to the core. There is water below and around the core, while a two-phase mixture of water exists on top. To capture the effects this effect, cross sections for water with conditions at the inlet was placed as an axial reflector 9 inches below the active fuel and ~12 inches (two extra radial nodes) on the periphery. In the case of the top axial reflector, homogenized cross-sections calculated at 80% void were used 9 inches above the fuel, since this is a representative void fraction for a BWR at hot operating conditions.

Peach Bottom Benchmark Results

The first benchmark performed of the Peach Bottom core was a test of initial conditions at start-up, without tracking the core through the entire first cycle. Using the given rod pattern at BOC, shown above, and the appropriate conditions of 55.7% rated power, 103.3% rated flow, with a bypass flow rate of 13.64 Mlbm/hr the first state point simulation was performed, which showed excellent initial agreement. The radial power distribution, shown below as Figure 4.11, gave very promising results. The peak radial power was ~1.33, where the rest of the radial power distribution demonstrated expected behavior. In the control cells where control blades were inserted, the center bundles of the core for example, the power was suppressed. In addition the power on the peripheral ring is low as well, and as expected, due to neutron leakage.

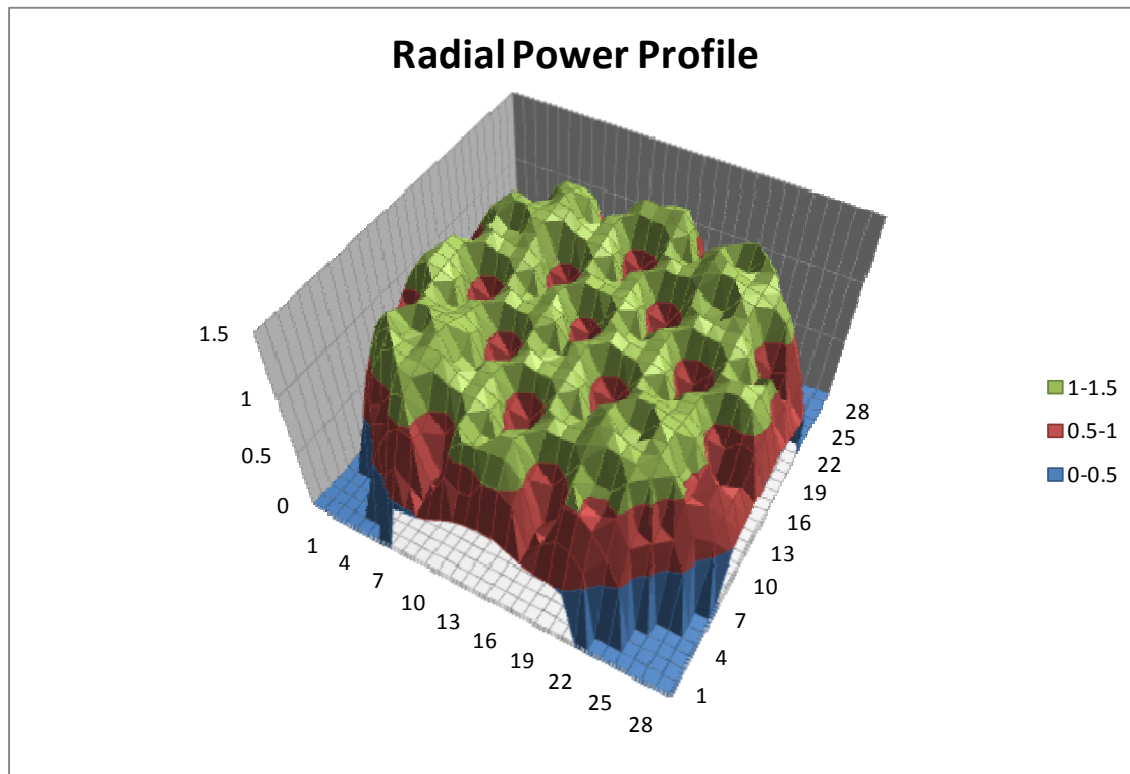


Figure 4.11 Peach Bottom Cycle 1 Radial Power Distribution

To ensure that the drift-flux model and flow redistribution model are working correctly, the channel by channel bundle flow matrix was checked to ensure several things. First, since the peripheral bundles have much smaller orifice diameters, the loss coefficient associated with it should serve to distribute less flow to the peripheral bundles, while diverting more flow to the central bundles. Secondly, since two-phase pressure losses are greater than single-phase pressure losses there should be more flow diverted to bundles in the presence of a control blade, and less flow to the bundles producing high power. In this sense, the flow map should be somewhat of an inverse mirror of the radial power map. Where there is high power, there should be lower flows and vice-versa. The attached Figure 4.12 shows the flow distribution throughout the core. Right away it noticed that the periphery does have lower flow rates on the order of 70% of core average flow while the bundles in the very center of the core, in the presence of a deep control

blade, demonstrate some of the highest flows; the flow distribution implementation appears to be working correctly.

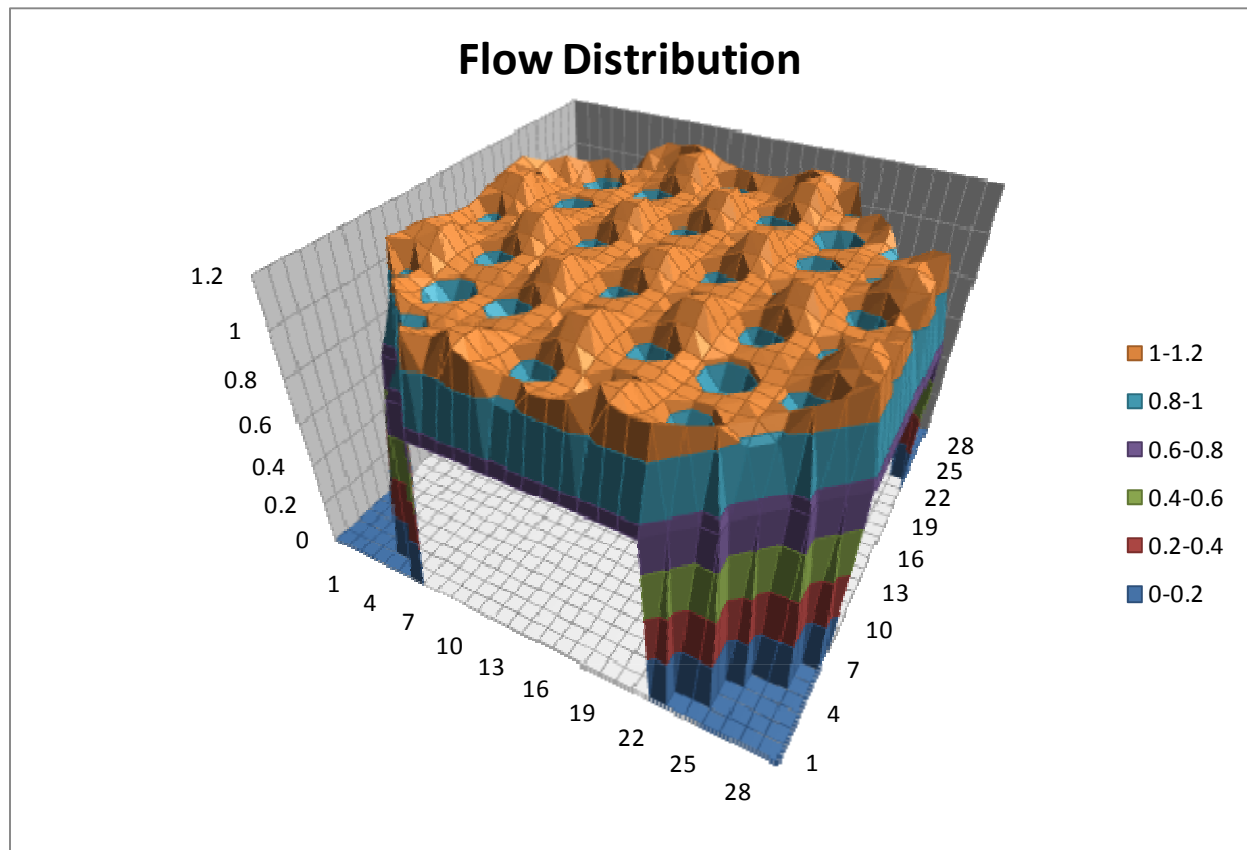


Figure 4.12 Peach Bottom Cycle 1 Core Flow Distribution

In addition to the radial features behaving as expected, axial variations also exhibited expected behaviors. Due to boiling in the core, typically BWR channels will see axial power profiles shifted to the bottom of the core, where neutron moderation is greater. This behavior is exhibited here in Figure 4.13, albeit with a double humped shape. While the neutron moderation is one factor affecting axial power profile, it is not the only one. Hence the bottom peaked power shape is illustrated, but there is also a distinct peak towards the top of the bundle. While this would seem counterintuitive given the discussion about void fraction and the affect on power, another factor coming in to play here is the axial fuel loading. The fuel bundle this occurs in has an axial loading pattern with a higher gadolinium fraction from 48 inches through to 84 inches. This

gadolinium loading profile mirrors the power suppression in the axial power profile as expected, with the power increasing again at the end of the fuel height loaded with higher gadolinium inventories.

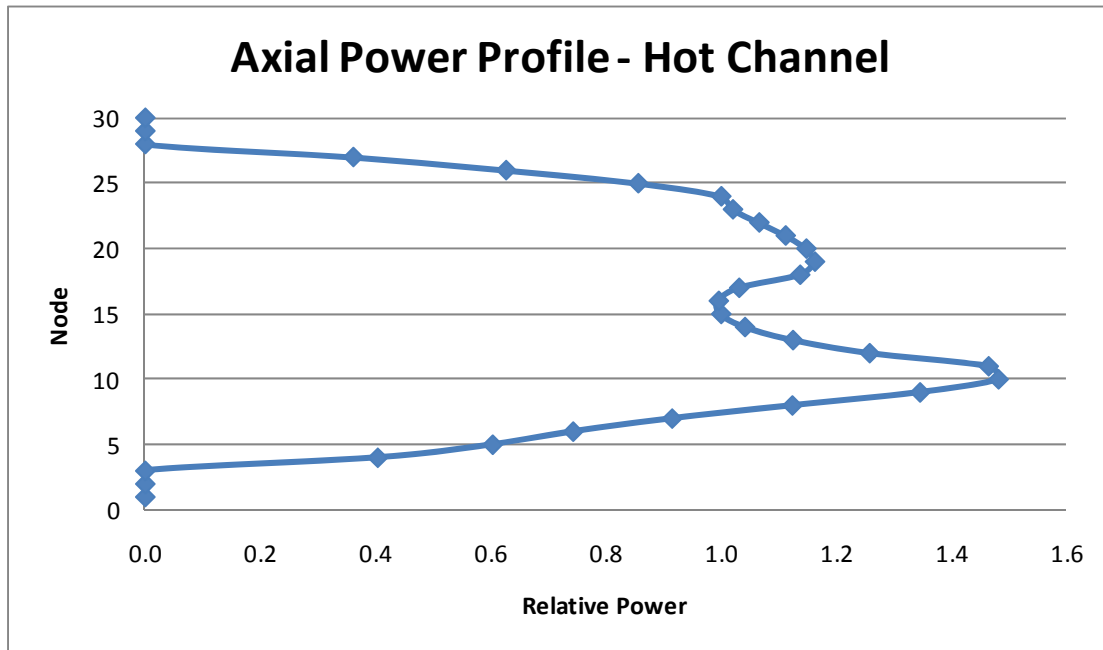


Figure 4.13 Axial Power Profile – Hot Channel

The axial void fraction for the most reactive channel is given below in Figure 4.14 for the channel corresponding to the axial power profile previously given. The first of several pertinent items, the 4 lowest nodes correspond to the lower axial reflector, thus no power is generated and no heating experienced. Following this, nodes 5-10 represent the first 36 inches of active fuel, whereupon the onset of boiling occurs after node 10. Also worth noting is that the peak void fraction does not reach 60% void, which appears low for the hot channel since void fractions of up to 80% are expected. The main reason for the suppression is the lower power state of the core coupled with high flow; running at ~55% of rated power yet greater than 100% flow rates will tend to cause this result.

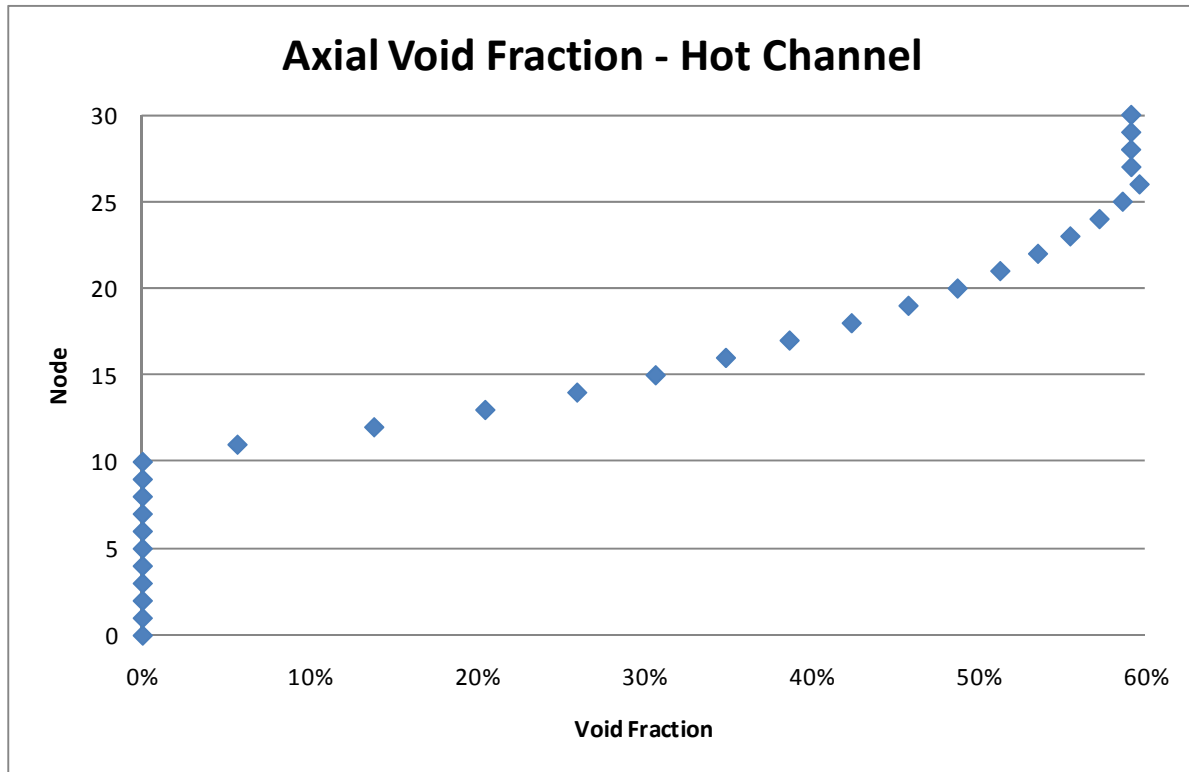


Figure 4.14 Axial Void Distribution – Hot Channel

When checking other major core parameters the benchmark shows favorable results. Until the full cycle 1 simulation is performed, complete with all control rod patterns and varying state points the TIP data cannot be analyzed to verify the power distribution, but upon the first pass several important parameters have been within expected ranges. The nodal power peak, defined as the ratio of the power in the most reactive node to the power in the average node, is calculated to be 2.0533, a very reasonable number for BWR operating conditions. Finally, since this core operating core data that is being compared against, the k_{eff} value throughout the cycle must be 1.00000. The accuracy to which the code predicts k_{eff} is one of the most important “catch all” parameters to benchmark against. The BOC calculation performed, once equilibrium Xenon and Samarium conditions are achieved, gave a value of 1.005934 for k_{eff} , indicating very good initial results. Once the burnup dependent cross-sections are available, the benchmark will be extended

to a full cycle 1 analysis and provide a more complete benchmark, but at the present time the results look very promising.

5. Implementation of Generalized Isotopic Tracking

This chapter largely includes items that are currently “work in progress” or still due to be completed by the end of this project. Subsections envisioned within this chapter are listed below:

Description of SCALE Lattice Physics Coupling to NESTLE

One of several major input requirements for NESTLE are collapsed macroscopic cross-section data. Historically three dimensional core simulators have been a two-fold code sequence where many lattice physics calculations are performed at various state points, in order to obtain cross-sections at a tight enough mesh to allow interpolation to be performed. Thus, for many BWR codes this mean running perhaps thousands of lattice physics runs. Running calculations at 0%, 20%, 40%, 60% and 80% void was required, at numerous burnup steps (with smaller BOC steps due to the presence of gadolinium), including restart conditions at each state point; where rodged and unrodged conditions also need to be considered. NESTLE is somewhat unique in the sense that the code accepts cross-sections tabulated in a different form. Lattice physics runs are performed at many of the conditions described above, but instead of bringing in the raw data, polynomial fits are applied to the data, with a given cross-section used as the “base” cross-section. Thus the amount of data required to be accounted for is much smaller and the cross-section files are not as large.

In the SCALE version of NESTLE the lattice physics code used to perform cross-section calculations is TRITON. TRITON input decks are created for the various fuel lattices required for a given fuel bundle design, allowing the user many degrees of freedom regarding how refined the mesh is, the energy group structure as well as many other options. Once the lattice runs are completed and collapsed homogenized cross-sections at each state point are available, a code called “T2N”, which stands for “TRITON to NESTLE” is executed which performs polynomial fitting calculations, and generates a cross-section file compatible with NESTLE for each lattice

type required. Once each lattice has a unique NESTLE compatible cross-section file, these files are then compiled into one larger cross-section file which is used in the NESTLE calculations.

ORIGEN

An understanding of how ORIGEN performs calculations, including inputs calculations mechanisms, what inputs are required as well as potential add-ons that would be beneficial within the scope of a 3-D core simulator will be undertaken. Prior to actually calling ORIGEN on a node-by-node basis a thorough understanding of what is needed and potentially what additional information would server helpful will be grasped.

Coupling ORIGEN to NESTLE

Once ORIGEN is sufficiently understood, the task of calling ORIGEN node-by-node, at each burnup step will be undertaken. Understanding where NESTLE performs depletion calculations, and where the ORIGEN call will best fit in is important. In addition, as a simulation is performed, the output of one burnup step will become the input to the next burnup step for isotopic information (among other required inputs), thus an understanding of how to create the input requirements for ORIGEN from the output of the previous step will be required for correct implementation.

End to End Demonstration of Actinide Recycling Illustrations

Once ORIGEN has been fully integrated into the NESTLE code, a demonstration of the capabilities of the new code suite will be performed. Using bundles spiked with Americium loaded into the core, the tracking of the full suite of actinides will be shown and compared against those of a standard bundle in the same locations. A much greater understanding of the path of ²⁴¹Am transmutation can be gleaned from this simulation, as the net accumulation of all the various actinides can be compared against the reference bundle.

In addition, a full code end-to-end demonstration will be performed, which include the creation of an optimum fuel lattice loading pattern, using the bundle design described in chapter 2, to the TRITON simulation of this lattice, to the “T2N” conversion of the cross-section to a NESTLE

compatible format, to a final execution of the TRITON code including tracking of all actinides will be performed to showcase the newly developed capabilities.

6. References

- [1] A. Ansari, *et al.* "FIBWR: A Steady-State Core Flow Distribution Code for Boiling Water Reactors – Computer Code Manual", EPRI NP-1924-CCM, Electric Power Research Institute (1981).
- [2] B. Chexal, G. Lellouche, "A Full Range Drift-Flux Correlation for Vertical Flows", EPRI NP-3989-SR (1986).
- [3] E. D. Collins, G. D. DelCul, J. P. Renier, B. B. Spencer, "Preliminary Multicycle Transuranic Actinide Partitioning-Transmutation Studies", ORNL/TM-2007/24, February 2007.
- [4] E.D. Collins, J.P. Renier, "Comparative Evaluation of TRU Actinide Transmutation in Fast and Thermal Burner Reactors", *Trans. Am. Nucl. Soc.*, **95**, 224-226, (2006).
- [5] M. Erighin, C. Yin, J. Galloway, G. I. Maldonado, "Analysis of BWR Lattices to Recycle Americium," *PHYSOR-2006, ANS Topical Meeting on Reactor Physics Organized and hosted by the CNS*, Vancouver, BC, Canada, D063, 1-10/10, Sept. 10-14, 2006.
- [6] Fioni G., Cribier M., Marie F., Aubert M., Ayrault S., Bolognese T., Cavedon J.-M., Chartier F., Deruelle O., Doneddu F., Faust H., Gaudry A., Gunsing F., Leconte P., Lelievre F., Martino J., Oliver R., Pluquet A., Rottger S., Spiro M., Veyssiere C., "Incineration of ^{241}Am Induced by Thermal Neutrons", *Nuclear Physics A*, **Volume 693**, Number 3, 22 October 2001, pp. 546-564(19).
- [7] Francois, J.L., Guzman, R. "BWR Fuel Design Using Minor Actinides as Burnable Absorber", *Trans. Am. Nucl. Soc.*, **96**, 748-749, (2007).
- [8] I. Gauld, O.W. Hermann, R.M. Westfall, "ORIGEN-S Scale System Module to Calculate Fuel Depletion, Actinide Transmutation, Fission Product Buildup and Decay, and Associated Radiation Terms", ORNL/TM-2005/39, Version 6, Vol. II, Sect. F7, (2009).

- [9] Gluck, M. (2008). "Validation of the sub-channel code F-COBRA-TF Part I. Recalculation of single-phase and two-phase pressure loss measurements" *Nuclear Engineering and Design*. **238**, 2308.
- [10] H. Hernandez, and G.I. Maldonado, "Application of Simulated Annealing Optimization to Recycle Minor Actinides in a BWR Lattice," *Trans. Am. Nucl. Soc.*, **96**, 771-773 (2007)
- [11] H. Hernandez and G. I. Maldonado, "Added Features and MPI-based Parallelization of the FORMOSA-L Lattice Loading Optimization Code," Proceedings of ANS Advances in Nuclear Fuel Management IV, Hilton Head Island, SC, 2009.
- [12] V.N. Koscheev, G.N. Manturov, M.N. Nikolaev, A.M. Tsiboulia, S.M. Bedniakov, V.A. Dulin, Yu. S. Khomiakov, "Nuclear Data for Plutonium and Minor Actinides", Proc. 3d Conf. on Accelerator Driven Transmutation Technology, Report We-I-15, Prague, (1999).
- [13] R. Lahey and F. Moody, *The Thermal Hydraulics of a Boiling Water Nuclear Reactor*, American Nuclear Society, La Grange Park, IL (1977).
- [14] N.H. Larson, "Core Design and Operating Data for Cycles 1 and 2 of Peach Bottom 2", Electric Power Research Institute (EPRI), (1978).
- [15] G. Lellouche and B. Zolotar, "Mechanistic Model for Predicting Two-Phase Void Fraction in Vertical Tubes, Channels, and Rod Bundles", EPRI NP-2246-SR (1982).
- [16] G. I. Maldonado, J. Galloway, H. Hernandez, K. T. Clarno, E. L. Popov, M. A. Jessee, "Integration of the NESTLE Core Simulator with SCALE", *Trans. Am. Nucl. Soc.*, **100**, 619-620, (2009).
- [17] B.R. Moore, "Higher Order Generalized Perturbation Theory for In-Core Nuclear Fuel Management Optimization", Ph D. Dissertation North Carolina State University, 1996.
- [18] B. Neykov, F. Aydogan, L. Hochreiter, K. Ivanov (PSU), H. Utsuno, K. Fumio (JNES), E.Sartori (OECD/NEA) "NUPEC BWR Full-Size Fine-Mesh Bundle Test (BFBT)

Benchmark, Volume I: Specifications”, OECD 2006, NEA No. 6212, NEA/NSC/DOC(2005)5, ISBN 92-64-01088-2 (2006).

- [19] D. Poston, H. Trellue, “User’s Manual, Version 2.0 for MONTEBURNS” Version 1.0. LA-UR-99-4999.
- [20] G. Raites, M. Todosow, A. Aronson, A. Galperin (Ben-Gurion University of the Negev), “Initial Studies of Transmutation Options for Boiling-Water Reactors”, BNL-AFCI-2005-002, Brookhaven National Laboratory, September 30, 2005.
- [21] D. Reddy, S. Sreepada, and A. Nahavandi, “Two-Phase Friction Multiplier Correction for High-Pressure Steam-Water Flow”, EPRI NP-2522, Electric Power Research Institute (1982).
- [22] The RELAP5-3D Code Development Team, “RELAP5-3D Code Manual Volume 1: Code Structure, System Models and Solution Methods”, INEEL-EXT-98-00834, Revision 1.3a, February (2001).
- [23] P. Saha and N. Zuber, “Point of Net Vapor Generation and Vapor Void Fraction in Subcooled Boiling”, in *Proc. 5th. International Heat Transfer Conference*, Tokyo, Japan, p. B4.7 (1975).
- [24] B.S. Shiralkar, D.W. Radcliffe, 1971. “An experimental and analytical study of the synthesis of grid spacer loss coefficients”, General Electric Technical Report NEDE-13181.
- [25] M. Stalek, C. Demaziere, “Development and Validation of a cross-section interface for PARCS”, *Annals of Nuclear Energy*, **35**, 2397-2409, (2008).
- [26] Taiwo, T.R. and Hill, R.N, “Comprehensive Summary of AAA and AFCI Transmutation Analysis Studies,” ANL-AFCI-198, September 30, 2007.
- [27] P. J. Turinsky, R. M. Al-Chalabi, P. Engrand, H. N. Sarsour, F. X. Faure and W. Guo, "Code Abstract - NESTLE: A Few-Group Neutron Diffusion Equation Solver Utilizing the

Nodal Expansion Method for Eigenvalue, Adjoint, Fixed-Source Steady-State and Transient Problems," *Nucl. Sci. & Engr.*, **120**, 72, 1995.

- [28] Varaine, Frederic, Zaetta, Alain. "Transmutation in Nuclear Reactors: Scientific and Technical Feasibilities Aspect", *Trans. Am. Nucl. Soc.*, **96**, 736-738, (2007).
- [29] Y. Xu, T. Downar, R. Walls, K. Ivanov, J. Staudenmeier, J. March-Lueba, "Application of TRACE/PARCS to BWR Stability Analysis", *Annals of Nuclear Energy*, **36 Issue 3**, 317-323, (2009).
- [30] A. Zaetta, "Prospective of LWRs to Reduce Minor Actinide Inventories", Nuclear Science Committee Meeting, Paris, June 9-11 (2004).
- [31] N. Zuber and J. Findlay, "Average Volumetric Concentration in Two-Phase Flow Systems", *J. Heat Transfer*, **87**, 453 (1965).

Budget Data (as of date):

This project has expended its original budget. Project is being finalized under a no-cost status.